Development of Thermoelectric Transport Measurement Schemes in Graphene Heterostructures

Master's Thesis

in the Degree Program
"Master of Science"
in Applied and Engineering Physics

at the Department of Physics
of the Technical University of Munich

by
Hajar Mouqadem

Supervisors:

Prof. Dr. Alexander Holleitner
Prof. Dr. Dmitri K. Efetov
Dr. Giorgio di Battista

Munich 2025

Acknowledgements

I would like to express my heartfelt gratitude to Prof. Dr. Dmitri K. Efetov for providing me with the opportunity to work in his lab on such an exciting project. I am deeply thankful to Dr. Giorgio di Battista for his constant supervision, guidance, and for always being available for insightful discussions. I am also grateful to Prof. Dr. Alexander Holleitner for his valuable feedback throughout my work, as well as to Prof. Dr. Martin S. Brandt for reviewing my thesis. I would also like to thank Prof. Dr. Michael Scherer, who first introduced me to this fascinating field of 2D materials during my bachelor's thesis and kindly referred me to this group.

A special thanks to the members of the TBG subgroup, particularly Leon, for providing me with my initial training in the fab in such a lighthearted and approachable way. I also appreciate the discussions and collaboration with the rest of the team. A special note of gratitude goes to Prof. Dr. Martin Lee for his constant readiness to help. Many thanks to the technicians Philipp and Christian for their constant willingness to assist us at all times. A sincere thank you to all the members of the group for their encouragement and support, and for making this year so memorable, full of science, events, and laughter.

I want to thank Aya, Imane and Mehdi for their help and presence throughout this journey, and most importantly, to Simo, whose unwavering support, belief in me, and constant presence through both the ups and downs have meant the world to me and kept me going. Last but not least, I want to thank my parents for their immeasurable support in every aspect of my life, enabling me to pursue my dream of studying physics.

ABSTRACT

This thesis develops a measurement scheme for investigating the thermoelectric properties of graphene devices, with a focus on twisted bilayer graphene. Bilayer graphene, when twisted near the magic angle of 1.1°, exhibits a range of unconventional phenomena, including correlated insulators and superconductivity, driven by electron-electron interactions within flat bands. While electrical transport has been the primary method for studying these behaviors, thermoelectric measurements provide additional insights into the particle-hole asymmetry in the density of states. We fabricate several graphene devices to optimize the thermoelectric measurement scheme, employing on-stack gold microheaters to generate the temperature gradient. The Seebeck voltage is measured and analyzed with respect to various measurement parameters, with results compared to the Mott formula. Deviations are observed at specific carrier densities, suggesting further areas for investigation. This work lays the groundwork for more advanced thermoelectric measurements in the group and future exploration of the thermoelectric properties of correlated states in magic-angle twisted bilayer graphene.

Contents

1 Introduction

When two identical graphene layers are stacked with a small twist angle relative to each other, a new periodic structure, known as the Moiré pattern, emerges. This pattern, characterized by a much larger periodicity compared to single-layer graphene, significantly modifies the properties of this new class of twisted two-dimensional materials. Near the magic angle of approximately 1.1°, twisted bilayer graphene (TBG) presents a fascinating platform for studying a wide range of unconventional physical phenomena [1], such as interaction-driven states (e.g., correlated insulators [2]), superconductivity [3], and topological phases [4]. These emergent behaviors are largely attributed to enhanced electron-electron correlations within the flat bands that arise at this specific twist angle, where the reduction in the kinetic energy of the electrons amplifies many-body interactions. Electrical transport has been the primary method for understanding these phenomena, where the device's resistance is analyzed as a function of various physical parameters. However, thermoelectric transport offers an additional, complementary probe, providing insights into the system that are not accessible via electrical transport alone [5–7]. Specifically, the Seebeck coefficient, or thermopower, is a sensitive indicator of the particle-hole asymmetry in a solid, as its sign depends on the dominant carrier type involved in transport. In Ref. [5], it was observed that the thermopower in magic-angle twisted bilayer graphene (MATBG) shows fully positive or negative values at states where it is expected to reset to zero, signaling an asymmetry in the density of states.

To further exploit this probe, this thesis develops and implements a reliable measurement scheme for performing thermoelectric measurements on graphene devices. Several graphene devices were fabricated to test well-established measurement techniques and refine them for our purposes. The thesis is organized as follows: In Chapter 2, we begin by exploring the physics of thermoelectricity within a semi-classical framework, followed by a brief overview of the properties of both single-layer and twisted bilayer graphene. This combined information will help us predict the expected response from our measurements. In Chapter 3, the fabrication and design of the devices are detailed, with a particular focus on the fabrication steps that enabled a successful measurement scheme, especially regarding the gold microheaters that create the temperature gradient necessary for thermoelectric experiments. The section concludes with a description of the measurement technique employed, as well as preliminary tests on single-layer graphene devices, which helped structure the subsequent measurements on the main twisted bilayer graphene device. In Chapter 4, electrical transport measurements are conducted to determine the twist angle of the TBG device, assess its homogeneity, and identify the existing states within it. Then, in Chapter 5, an in-depth analysis of the heating scheme induced by the heater is

provided, exploiting the temperature dependence of the half-filled correlated state present in the device. Using this information, we determine the Seebeck coefficient and further optimize the thermovoltage signal with respect to key measurement parameters. Finally, in Section 5.3, we compare the optimized measurements with the theoretically predicted baseline model and briefly discuss any deviations. Last but not least, the most recent data, featuring both longitudinal and transverse thermovoltage responses in the presence of a magnetic field, is presented, setting the stage for for future in-depth analysis as a continuation of this project.

2 Theoretical background

In this chapter, we present the theoretical basis necessary to understand the experimental results discussed in this thesis, in particular the thermoelectric response of graphene devices. After introducing the Seebeck effect and deriving its formulation within the semi-classical Boltzmann picture, we provide a brief overview of the lattice structure and electronic band structure of graphene and twisted bilayer graphene.

2.1 The Seebeck effect

The following discussion is based on the book by Kamran [8].

2.1.1 A brief introduction to thermoelectricity

Thermoelectricity refers to the interplay between heat and charge transport in a material. From Ohm's law for electrical transport, a charge current is generated when applying an electric field through an electrical conductor (a metal), where the electrical conductivity σ quantifies how well the metal conducts current:

$$\boldsymbol{J_e} = \sigma \boldsymbol{E}. \tag{2.1}$$

Similarly for thermal transport, a temperature gradient causes a heat current and the corresponding quantity is the thermal conductivity κ:

$$\boldsymbol{J_q} = -\kappa \boldsymbol{\nabla} T. \tag{2.2}$$

In the 19th century, Seebeck and Peltier made observations that revealed a link between electrical and thermal transport: Seebeck found that a voltage difference is generated between two wires when heating the junction between them, and Peltier detected a temperature difference when sending an electrical current across the junction of two metals. These phenomena can be understood by introducing two other conductivities α and β such that:

$$\boldsymbol{J_e} = \sigma \boldsymbol{E} - \alpha \boldsymbol{\nabla} T, \tag{2.3}$$

$$\boldsymbol{J_q} = \beta \boldsymbol{E} - \kappa \boldsymbol{\nabla} T. \tag{2.4}$$

The first equation means that a charge current can be generated not only by an electric field but also a temperature gradient, with corresponding thermoelectric conductivity

α. Similarly, the second equation tells that in addition to a temperature gradient, heat current can also be induced by an electric field, with "electrothermal" conductivity β. However, it was argued by Lord Kelvin, and later proven by Onsager that these two new quantities are not independent and are related through

$$\beta = \alpha T, \tag{2.5}$$

such that we are left with only three distinct conductivities: σ, κ and α. We now can understand what Seebeck had observed: in the absence of a charge current $\boldsymbol{J_e} = 0$, Eq. 2.3 tells us that a temperature gradient induces an electric field, and thus an open-circuit electrical voltage. The Seebeck coefficient S (also referred to as thermopower) is defined as the ratio between the induced electrical field and the temperature gradient

$$S = -\frac{E}{\nabla T} = -\frac{\alpha}{\sigma}. \tag{2.6}$$

The minus sign comes from the typical sign convention used in the community, where a positive/negative Seebeck coefficient corresponds to positive/negative charge carriers respectively. As we will see, unlike σ and κ which are always positive, S can be either positive or negative depending on the dominant carrier type. In experiments, the Seebeck coefficient is measured by imposing a temperature difference ΔT along the sample and measuring the resulting voltage ΔV such that

$$S = -\frac{\Delta V}{\Delta T}. \tag{2.7}$$

Here, the length cancels out since the temperature gradient and the electric field share the same length scale. The magnitude of the Seebeck coefficient is usually in the order of $\mu\mathrm{V\,K^{-1}}$.

2.1.2 Semi-classical description of the Seebeck coefficient

Electrons in a solid follow the Fermi-Dirac energy distribution

$$f^0(\varepsilon) = \frac{1}{e^{\frac{\varepsilon-\mu}{k_B T}} + 1}, \tag{2.8}$$

where μ is the chemical potential, i.e., the energy required to add an electron to the system. At the zero-temperature limit, the Fermi-Dirac distribution becomes a step function, where all energy levels below the Fermi energy $\varepsilon_F = \mu(T = 0)$ are occupied and all energies above it are unoccupied. At finite temperatures, the distribution is thermally broadened, and electrons with energies both lower and higher than the chemical potential can be found

with finite probability (Fig. 2.1). This property, combined with Boltzmann transport theory, will provide energy-dependent expressions for the above-discussed conductivities, and thus for the Seebeck coefficient.

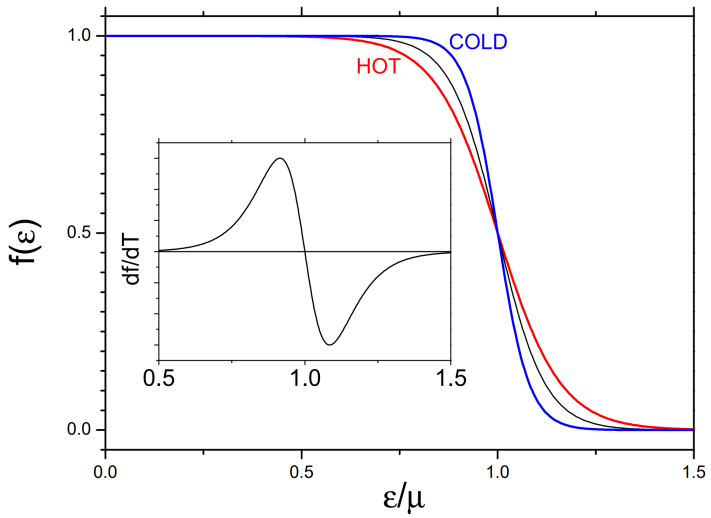

Figure 2.1: Thermal broadening of the Fermi-Dirac distribution in the presence of a small temperature gradient, where the the distribution is sharper on the cold side and broader on the hot side. The inset shows the temperature derivative of the distribution df/dT, which is antisymmetric with respect to $\varepsilon - \mu$. The image is taken from Ref. [9], licensed under CC BY 4.0.

In the Boltzmann approach, one considers the function $f_{\mathbf{k}}(\boldsymbol{r})$ which represents the probability of finding an electron with wave-vector $\boldsymbol{k}$ at position $\boldsymbol{r}$. In the absence of an electric field or a temperature gradient, this function is equal to the Fermi-Dirac distribution f^0. When the system is perturbed by an electric field, by a temperature gradient or by scattering events, the Boltzmann equation states that $f_{\mathbf{k}}(\boldsymbol{r})$ deviates from f_0 such that these three contributions cancel out. In the linear regime approximation, where the deviation from f_0 is small, the following, additional approximations lead to the linearized Boltzmann equation:

- $f_{\mathbf{k}}(\boldsymbol{r})$ relaxes back to the equilibrium distribution over a characteristic scattering time τ

$$\frac{df_{\mathbf{k}}(\boldsymbol{r})}{dt}|_{\text{scattering}} = \frac{f_{\mathbf{k}}(\boldsymbol{r}) - f^0}{\tau} \tag{2.9}$$

- The only effect of the temperature gradient is the thermal broadening of the Fermi-Dirac distribution in a small energy window ($\Delta T \ll T$):

$$\frac{df_{\mathbf{k}}(\boldsymbol{r})}{dt}|_{\nabla T} = \boldsymbol{v}_{\mathbf{k}} \cdot \frac{\partial f_{\mathbf{k}}}{\partial \boldsymbol{r}} \approx v_{\mathbf{k}} \frac{\partial f^0}{\partial T} \nabla T, \tag{2.10}$$

where $\boldsymbol{v}_{\mathbf{k}} = \frac{\mathrm{d}\boldsymbol{r}}{\mathrm{d}t} = \frac{1}{\hbar}\frac{\partial \varepsilon_{\mathbf{k}}}{\partial \mathbf{k}}$ is the group velocity of the electron. Similarly for the electric

field $\boldsymbol{E}$:

$$\frac{df_{\mathbf{k}}(\boldsymbol{r})}{dt}|_{\boldsymbol{E}} = \frac{e}{\hbar}\boldsymbol{E}\cdot\frac{\partial f_{\mathbf{k}}}{\partial \mathbf{k}} \approx ev_{\mathbf{k}}\frac{\partial f^0}{\partial \epsilon_{\mathbf{k}}}E, \tag{2.11}$$

with $e\boldsymbol{E} = \hbar\frac{d\boldsymbol{k}}{dt}$.

Canceling out these three contributions gives the linearized Boltzmann equation

$$v_{\mathbf{k}}\frac{\partial f^0}{\partial T}\nabla T + ev_{\mathbf{k}}\frac{\partial f^0}{\partial \varepsilon_{\mathbf{k}}}E + \frac{f_{\mathbf{k}}(\boldsymbol{r}) - f^0}{\tau} = 0. \tag{2.12}$$

Rearranging the equation, one can see that the local distribution deviates from its equilibrium f^0 by two perturbations:

$$f_{\mathbf{k}}(\boldsymbol{r}) = f^0 - \tau v_{\mathbf{k}}\left(\frac{\partial f^0}{\partial T}\nabla T + e\frac{\partial f^0}{\partial \varepsilon_{\mathbf{k}}}E\right). \tag{2.13}$$

Due to the different derivatives of f^0 in the above equation, the effect of the electric field is shifting the Fermi-Dirac distribution with respect to energy, while the effect of the temperature gradient is broadening it.
The electrical conductivity is found from setting $\nabla T = 0$, leaving only the electrical contribution in J_e:

$$J_e = \int v_{\mathbf{k}} e f_{\mathbf{k}} d\boldsymbol{k} \tag{2.14}$$

$$= \int \left(v_{\mathbf{k}} e f^0 - e^2\tau v_{\mathbf{k}}\cdot v_{\mathbf{k}}\frac{\partial f^0}{\partial \varepsilon_k}E\right) d\boldsymbol{k} \tag{2.15}$$

In steady-state, the average velocity is zero and the first integral vanishes. Comparing this equation with Eq. 2.3, one identifies

$$\sigma = -e^2\int \tau(\boldsymbol{k}) v_{\mathbf{k}}\cdot v_{\mathbf{k}}\frac{\partial f^0}{\partial \varepsilon_k} d\boldsymbol{k}. \tag{2.16}$$

Similarly, setting now the electric field to zero, we get

$$\alpha = -e\int \tau(\boldsymbol{k}) v_{\mathbf{k}}\cdot v_{\mathbf{k}}\frac{\partial f^0}{\partial T} d\boldsymbol{k}. \tag{2.17}$$

While both transport coefficients involve integrating over $\boldsymbol{k}$-space, the key difference lies in their "pondering factors" used in the averaging. The electrical conductivity σ is weighted by the energy derivative of the Fermi-Dirac distribution, $\partial f^0/\partial \varepsilon_{\mathbf{k}}$, which is symmetric about the chemical potential μ, and sharply peaked there. This symmetry ensures that contributions from states immediately above and below μ add constructively, leading to a positive conductivity regardless of any asymmetry in the electronic structure. In contrast, the thermoelectric conductivity α is weighted by the temperature derivative of

the equilibrium distribution, which can be expressed as

$$\frac{\partial f^0}{\partial t} = -\frac{\varepsilon - \mu}{T}\frac{\partial f^0}{\partial \varepsilon_k}. \tag{2.18}$$

This factor is odd with respect to $\varepsilon - \mu$ (Fig. 2.1): it changes sign when the energy deviates above or below μ. Consequently, if the rest of the integrand is symmetric around μ, the contributions from electrons (or holes) above μ cancel those from below, and α becomes zero. However, if there is an asymmetry in the electronic structure—such as in the density of states, group velocity, or scattering time—then the cancellation is incomplete, resulting in a finite thermoelectric response. The sign of α, and thus of the Seebeck coefficient $S = -\alpha/\sigma$, depends on the nature of this asymmetry: it will be positive if the asymmetry leads to a net transport of carriers with energies predominantly above μ (which is typical in n-type materials where electrons dominate), and negative if the carriers contributing are predominantly below μ (as is the case in p-type materials). Thus, while electrical conductivity is always positive, thermoelectric conductivity is highly sensitive to the detailed energy dependence of the electronic structure around the Fermi level, making it a sensitive probe in this sense.

2.1.3 Mott formula

In the Landauer formalism, which is equivalent to the above-discussed approach (see Ref. [8]), the two conductivities can be written as integrals over the energy instead of the wave-vector:

$$\sigma = -2\frac{e^2}{h}\int \frac{\partial f^0}{\partial \varepsilon_k}\Theta(\varepsilon)d\varepsilon, \tag{2.19}$$

$$\alpha = -\frac{2ek_B}{h}\int \frac{\varepsilon - \mu}{k_B T}\frac{\partial f^0}{\partial \varepsilon_k}\Theta(\varepsilon)d\varepsilon. \tag{2.20}$$

$\Theta(\varepsilon)$ is called transport distribution function and contains the scattering time and group velocity in addition to the density of states $g(\varepsilon)d\varepsilon = d^3k$. For a smooth function $\varepsilon(\mathbf{k})$:

$$\Theta(\varepsilon) = \frac{h}{2}g(\varepsilon)\tau(\boldsymbol{k})v_{\mathbf{k}} \cdot v_{\mathbf{k}} \tag{2.21}$$

A Sommerfeld expansion of the above integrals allows to transform them into development series in powers of k_BT/ε_F:

$$\sigma = 2\frac{e^2}{h}\left[\Theta(\varepsilon_F) + ...\right] \tag{2.22}$$

$$\alpha = 2\frac{\pi^2}{3}\frac{k_B e}{h}k_B T\left[\frac{\partial\Theta(\varepsilon_F)}{\partial\varepsilon}|_{\varepsilon=\varepsilon_F} + ...\right] \tag{2.23}$$

Comparing these two expressions reveals a link between electrical conductivity and thermoelectric conductivity in this semi-classical picture:

$$\alpha = \frac{\pi^2}{3}\frac{k_B^2}{e}T\frac{\partial\sigma}{\partial\varepsilon}|_{\varepsilon=\varepsilon_F} \tag{2.24}$$

This implies for the Seebeck coefficient, using $S = -\alpha/\sigma$

$$S = -\frac{\pi^2 k_B^2 T}{3e}\left.\frac{d\ln\sigma(\varepsilon)}{d\varepsilon}\right|_{\varepsilon=\varepsilon_F}. \tag{2.25}$$

This equation, known as the Mott formula, is widely used as a baseline model for interpreting thermoelectric measurements. When the measured or calculated Seebeck coefficient follows the trend predicted by the Mott formula, it suggests that the underlying assumptions are a reasonable approximation for the system. Conversely, deviations from the Mott formula can signal additional effects such as phonon-drag, inelastic scattering, strong correlations and other complex band structure features that require more advanced models [5, 6, 10, 11].

2.2 Graphene

Graphene is a two-dimensional material composed of carbon atoms arranged in a honeycomb lattice. Each carbon atom is sp^2 hybridized, forming three strong in-plane σ bonds with neighboring atoms. The remaining unhybridized $2p_z$ orbital extends out of the plane, forming a delocalized π-electron system [12]. The honeycomb lattice corresponds to a hexagonal Bravais lattice with a basis of two atoms per unit cell (Fig. 2.2a), with lattice constant a = 2.46 Å [13]. The corresponding Brillouin zone is described by reciprocal lattice vectors $\boldsymbol{b_i}$ that satisfy $\boldsymbol{b_i}\cdot\boldsymbol{a_j} = 2\pi\delta_{ij}$, where $\boldsymbol{a_j}$ are the real space vectors (Fig. 2.2b).

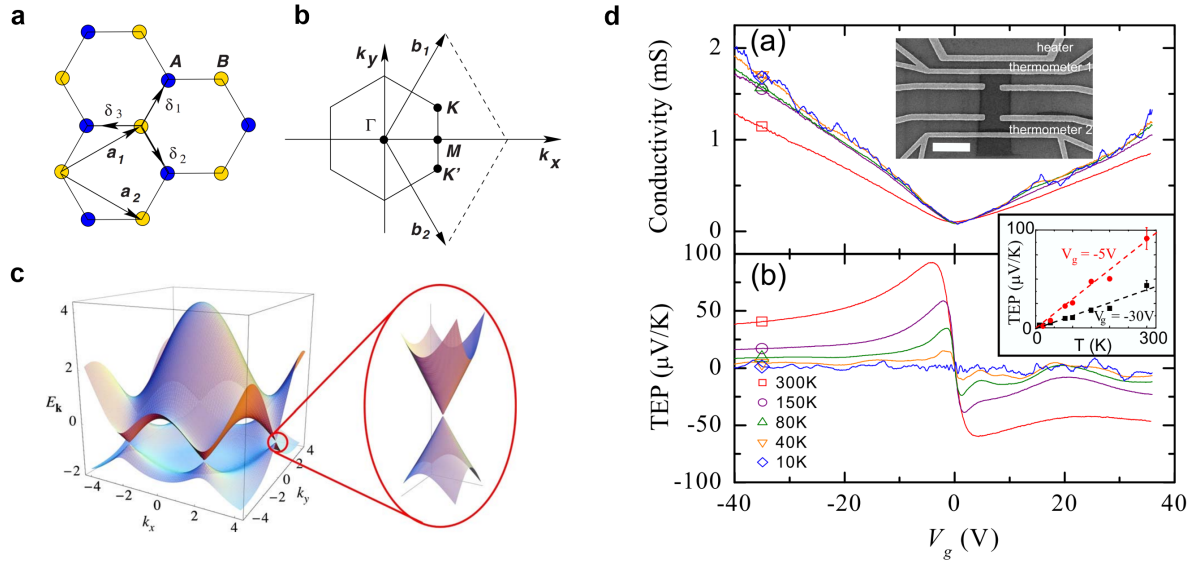

Figure 2.2: Electronic structure of graphene. **a**, Honeycomb lattice of graphene in real space. **b**, Corresponding Brillouin zone in reciprocal space with high-symmetry points K, K' and M. **c**, Calculated electronic structure of graphene using the tight-binding model and zoomed-in view of the energy bands near one of the Dirac points. **d**, Top panel: Measured conductance vs. gate voltage in a graphene sample, showing the characteristic dip at charge neutrality. Bottom panel: Measured thermopower vs. gate voltage at different temperatures showing the characteristic S-shape for graphene. Figures **a** to **c** are reprinted from [12] and **d** is reprinted from [14] with permission. Copyright (2009), (2009) respectively by the American Physical Society.

The electronic band structure of graphene can be analytically calculated using the tight-binding model, which assumes that electrons are primarily localized around atoms and can hop to adjacent lattice sites. Considering only nearest-neighbor hopping with hopping amplitude t, the solution of the tight-binding Hamiltonian yields the following energy dispersion relation [12]:

$$E_{\pm}(\boldsymbol{k}) = \pm t\sqrt{3 + 2\cos\left(\sqrt{3}k_y a\right) + 4\cos\left(\frac{\sqrt{3}k_y a}{2}\right)\cos\left(\frac{3k_x a}{2}\right)} \tag{2.26}$$

Near the corners of the Brillouin zone, called the Dirac points or valleys K and K', the dispersion becomes linear:

$$E_{\pm}(\boldsymbol{q}) = \pm\hbar v_F|\boldsymbol{q}|. \tag{2.27}$$

$\boldsymbol{q}$ is the momentum measured from the Dirac point and $v_F \approx 1 \times 10^6\,\mathrm{m\,s^{-1}}$ is the Fermi velocity. This results in a conical band structure where the conduction and valence bands meet at the Dirac point (Fig. 2.2c). At these points, the energy gap between the bands is zero, resulting in a "band crossing" and making graphene a semi-metal. Additionally, electrons near the Dirac point (or charge-neutrality point) behave as massless

Dirac fermions [12]. These properties manifest in electrical transport experiments as a characteristic resistance peak (or conductance minimum) when the carrier density is tuned such that the Fermi level lies at the charge neutrality point. In thermoelectric experiments, the Seebeck coefficient displays an S-shaped dependence on carrier density (Fig. 2.2d): it is positive for hole doping, negative for electron doping, and crosses zero at the Dirac point, reflecting the particle-hole symmetry of the linear band structure.

2.3 (Magic-angle) twisted bilayer graphene

Stacking two identical graphene layers with a small relative twist angle generates a periodic Moiré pattern that reflects a long-range modulation of the local stacking order (Fig. 2.3a) [2]. We refer to this new periodic structure as twisted bilayer graphene (TBG). From geometrical considerations and for small, commensurate twist angles, its lattice constant is given by [15]

$$L_M \approx \frac{a_0}{2\sin(\theta/2)}, \tag{2.28}$$

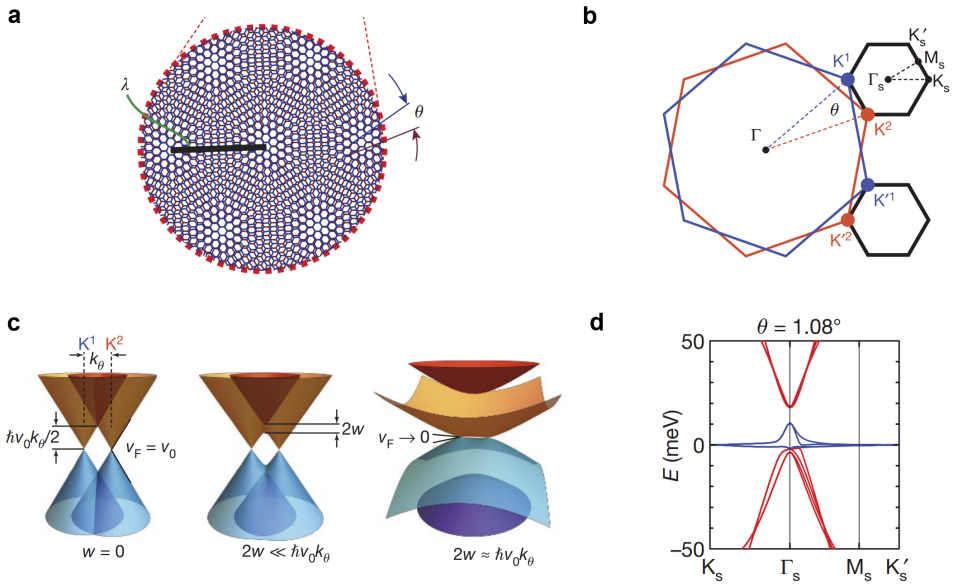

Figure 2.3: Magic-angle twisted bilayer graphene. **a**, Periodic Moiré pattern induced by twisting two identical graphene layers with a small, relative twist angle. **b**, Mini Brillouin zones constructed from the difference between the valleys of each layer, corresponding to the Moiré superlattice **c**, Interlayer hybridization for $w = 0$, $2w \ll \hbar v_0 k_\theta$ and $2w \approx \hbar v_0 k_\theta$. The latter case gives rise to flat bands with reduced Fermi velocity. **d**, Calculated band structure for magic-angle $\theta = 1.08°$, where the flat band is shown in blue. The figures are from Ref. [2], reproduced with permission from Springer Nature.

where a_0 is the lattice constant of monolayer graphene and θ is the twist angle. Small twist angles result in a "superlattice" unit cell many times larger than the unit cell of a single layer (e.g. L_M is 60 times larger than a_0 for $\theta = 1°$), resulting in, new, small "mini Brillouin zones" in reciprocal space. The area of the superlattice cell is given by [15]

$$A_s = \frac{\sqrt{3}}{2} L_m^2 = \frac{\sqrt{3} a_0^2}{8 \sin^2(\theta/2)}. \tag{2.29}$$

In simplistic terms and based on the description in [2], the band structure of TBG can be understood by considering two sets of single-layer graphene Dirac cones rotated about the Γ point in the Brillouin zone by the twist angle θ (Fig. 2.3b)[2]. The new, mini Brillouin zones are constructed from the difference between K^1 and K^2 (or K'^1 and K'^2), where 1 and 2 refer to the valleys of single-layer 1 and single-layer 2 respectively. Within one mini Brillouin zone, interlayer hybridization due to interlayer hopping between the two layers leads to valley mixing between the closest Dirac cones, e.g. K^1 and K^2 in Fig. 2.3b, while interactions between distant Dirac cones are suppressed exponentially. This twist-angle dependent hybridization leads to the emergence of low-energy flat bands with bandwidth less than 10 meV for a set of so-called "magic-angles" (Fig. 2.3 d).
As can be seen from Fig. 2.3c, the emergence of flat bands can be attributed to the competition between the kinetic energy $\hbar v_0 k_\theta$ (v_0 is the Fermi velocity of graphene) and the interlayer hybridization energy $2w$: the strongest hybridization of the bands occurs when $2w$ is comparable to the kinetic energy, leading to a suppression of the band dispersion near the Fermi level. The first magic-angle $\theta \approx 1.1°$ corresponds to a zero renormalized Fermi velocity v_F.

Within the flat bands, the kinetic energy is significantly reduced ($v_F \approx 0$), thereby enhacing electron-electron interactions and making the system highly susceptible to correlated electronic phases, such as unconventional superconductivity and insulating states, which are unique to MATBG. These phenomena are under extensive investigation using different probes such as electrical resistance measurements (Chapter 4) to identify insulating and superconducting states as well thermoelectric measurements (Chapter 5) to reveal potential asymmetries in the electronic structure and the origin of superconductivity.

3 Materials and methods

This chapter outlines the fabrication process of graphene devices, beginning with flake exfoliation and continuing through stacking, device design, and nanofabrication. The final section describes the experimental setup used for performing thermoelectric measurements on the fabricated devices.

3.1 Vertical assembly of van der Waals heterostructures

The core of the devices consists of hBN-encapsulated single-layer graphene or twisted bilayer graphene with a graphite back-gate. These two-dimensional materials can be vertically assembled (or "stacked") into a layered structure through van der Waals forces between them [16]. In this section, we describe the process of exfoliating the 2D layers from their bulk crystals, selecting flakes suitable for our device geometry, and assembling them using a modified dry-transfer technique developed by our group [17].

3.1.1 Exfoliation

Mechanical exfoliation is one of the most straightforward methods to obtain large, atomically thin flakes of high quality. In particular, few-layer and monolayer graphene as well as hBN flakes of ~10-20 nm thickness are exfoliated following the procedure established in [18], with some modifications made for hBN flakes [17] due to their tendency to break into smaller pieces more easily during the process. In the following, the exfoliation protocol for obtaining flakes similar to Fig. 3.2 is described.

Graphene exfoliation

To prepare the substrate into which the flakes will be transferred, we begin by cutting a silicon wafer coated with 285 nm of silicon dioxide into ~1x1 cm^2 chips such that as little silicon dust as possible lands on the chip surface. The surface is then flushed with a nitrogen gun to remove most of the dust. One can additionally sonicate the chips with acetone, isopropanol and deionized water. The 285 nm SiO_2 coating provides very good optical contrast, enabling the visualization of graphene (and hBN) flakes with an optical microscope and allowing for the immediate identification of monolayer graphene without the need for Raman spectroscopy [19].
The graphene flakes are exfoliated from a graphenium crystal using adhesive tape, as

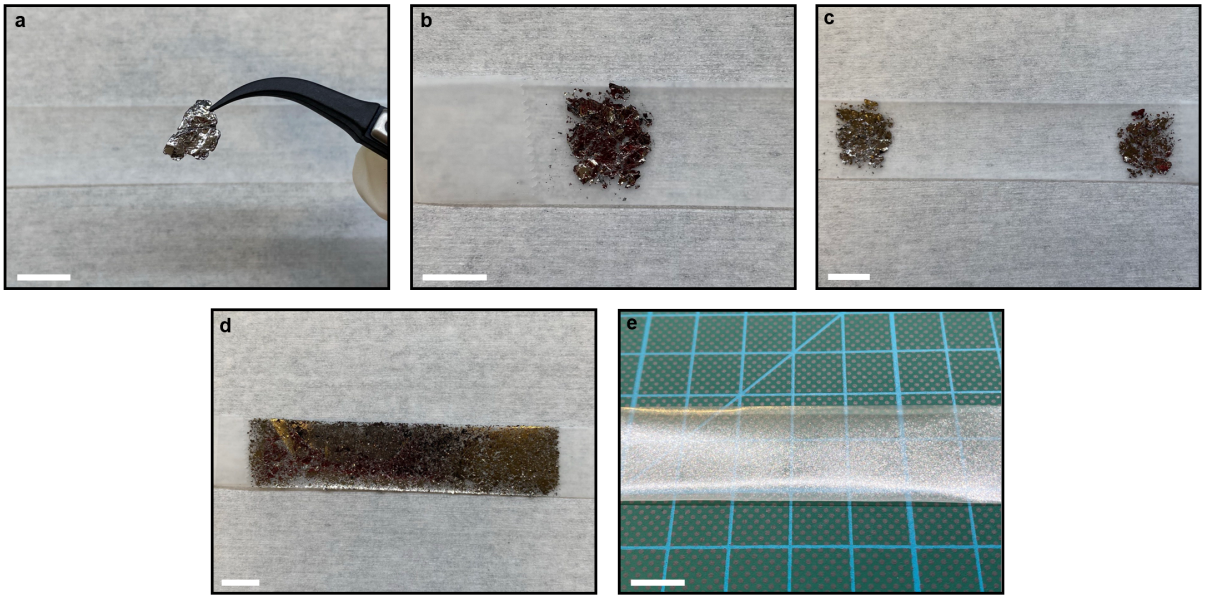

Figure 3.1: Scotch-tape exfoliation of graphene and hBN. a, Graphenium crystal. **b**, Placing the graphenium crystal on the scotch tape then removing it leaves large, thick graphite flakes on the tape. **c**, The tape is folded to create dense regions filled with thinner graphite flakes. **d-e**, Scotch tape ready for transfer of the graphene (**d**) and hBN (**e**) flakes to an SiO_2 substrate. The scale bar is 1 cm.

shown in Fig. 3.1a-d. First, the graphenium crystal is placed on a piece of tape then removed, leaving large pieces of graphite on the tape. In my experience, a shiny side of the crystal results in a more dense initial area of graphite. The tape is then folded several times to fill it with dense areas of thinned out graphite flakes. The rule of thumb is to minimize the number of folds to avoid breaking the flakes into overly small pieces, while obtaining areas of high density. This increases the chances of getting a monolayer and reduces the amount of tape residue during the transfer to the substrate.

Prior to the transfer, the Si/SiO_2 chips are cleaned with oxygen plasma to remove ambient adsorbates from their surface, enhancing the adhesion between the outermost graphene sheet and the substrate during transfer. They are then placed as quickly as possible on the prepared tape and pressed against it. The chips with the attached tape are then annealed at ~105 °C on a hot plate for 2 min, which further enhances the adhesion. Note that heating for too long will result in too much tape residue around the flakes. Finally, after the tape is cooled down to room temperature, the tape can be slowly and continuously peeled from the chips to avoid breaking of the flakes.

After the tape is removed, the competition of van der Waals forces acting between the graphene layers and the SiO_2 surface results in flakes with varying shapes and thicknesses on the chips. The criteria for selecting suitable flakes for our devices will be discussed further below in the Flake selection segment.

hBN exfoliation

The overall procedure and outcome of hBN exfoliation is the same as described above, however, due to the smaller size of the initial bulk hBN crystals, the following adjustments must be considered:

- Because the hBN flakes are more prone to breaking than graphene, more care must be taken when folding the tape and when peeling it off from the substrate. Additionally, less force should be applied when pressing the substrate against the tape.
- The hBN flakes obtained from the prepared tape are usually too thick for stacking. To thin them out, a second tape (daughter tape) is adhered to the original tape (mother tape) then carefully peeled off to avoid further breaking of the flakes. The daughter tape can then be used for transfer. More than one daughter tape can be made from one mother tape. Usually, a colorful tape indicates that the hBN has the optimal thickness to be exfoliated. If it is too shiny, then the flakes are too thick, and if it is not bright at all, they are too thin. A usable daughter tape is shown in Fig. 3.1e.
- Since the density of the hBN flakes is lower than in the case of graphene, the tape is not annealed to avoid having too much tape residue. Instead, the tape is left attached to the substrate for a few minutes before peeling it off.

3.1.2 Flake selection

Out of the multitude of flakes obtained from the exfoliation, we choose those suitable for making the graphene devices, which consist of an hBN-graphene-hBN-graphite stack at their core. The flakes are carefully selected to simultaneously contribute to a smooth stacking process, as well as satisfy requirements concerning device quality and geometric constraints that are necessary for both electrical and thermoelectric transport measurements, in particular the placement of gold microheaters to locally heat the graphene. In our approach, flake selection—along with the specific arrangement of the flakes (see Stack conception)—is crucial for achieving the target geometry. Another approach would be to place greater emphasis on nanofabrication, reducing restrictions on the choice of flakes and utilizing optimized etching to define the desired regions on the stack.
The following criteria apply to both single-layer and twisted bilayer graphene stacks, with additional considerations specific to TBG stacks.

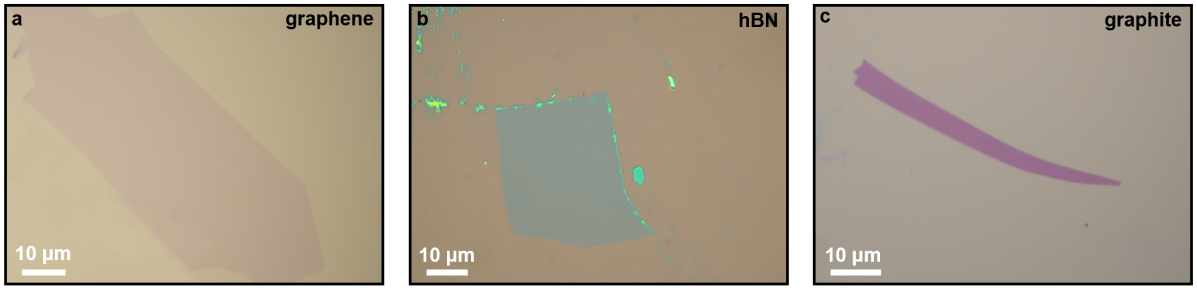

Figure 3.2: Desirable flakes for stacking. **a**, Large monolayer graphene flake free of visible defects. **b**, Homogeneous hBN flake with sharp edges and no thick flakes in its vicinity. **c**, Homogeneous, narrow and elongated graphite flake of optimal thickness.

Graphene flakes

We select clean graphene flakes with no visible defects such as in Fig. 3.2a. For making twisted bilayer graphene (TBG) stacks, the flake should be large enough to be cut into two roughly equal parts, as will be shown in the stacking section. Typical dimensions are ~10-20 µm in width and ~20-40 µm in length. It is relatively easy to find such flakes with the exfoliation protocol described above.

hBN flakes

The graphene will be fully encapsulated between a top and a bottom hBN flake, each serving multiple critical roles. The full encapsulation preserves the graphene and reduces contamination, for example from organic solvents during nanofabrication. Both hBN flakes are chosen to be homogeneous and free of defects that might cause the flakes to tear or fold during pick-up. Moreover, the presence of a nearby bulk region can complicate the pick-up process, making it preferable to choose isolated flakes. Since it is time-consuming to acquire an atomic force microscope (AFM) image for each selected flake, defects and step edges within the flakes can instead be identified optically by closing the aperture diaphragm of the microscope to increase the contrast, combined with appropriate LUTs adjustments [20]. For several reasons discussed below, flakes of ~15-20 µm thickness show to be optimal for our purposes.

The top hBN is used to pick the graphene up. It should be just big enough to fully cover the graphene flake. For TBG stacks, the top hBN should have at least one sharp edge to which the graphene edge will clamp, reducing the probability of twist angle relaxation (see Stacking process). The size and orientation of the top hBN with respect to the bottom hBN should be chosen as to have a graphite-bottom hBN-only region very close to the graphene edge, where the local gold microheaters will be placed. This is illustrated in Fig. 3.6 and explained in Subsection 3.2.1. Finally, using thinner hBN flakes in the above-mentioned range makes the pick-up smoother and allows to see the graphene flake

through the hBN.

Introducing a layer of hBN between the SiO_2 surface and the graphene significantly enhances the graphene mobility [21]. This is because hBN hosts fewer charge traps and exhibits less surface roughness. The bottom hBN also serves as a gate dielectric to the graphite back-gate (see next paragraph) that provides a capacitance at least ten times larger than that of a silicon gate, owing to its comparable dielectric constant and reduced thickness of ~15 nm compared to 285 nm for SiO_2. However, flakes that are too thin are undesirable as they can cause leakage currents.
As mentioned previously, the gold microheaters are evaporated on the graphite-bottom hBN region. Here again, the bottom hBN should not be too thin, because it provides electrical insulation between the gold and the graphite gate. On top of that, a too thin flake might cause the narrow heaters to break, as was observed in one of the devices (see Fig. 3.9D2). Another reason why we choose flakes in the range of 15–20 nm, rather than thicker ones, is the assumption that heat from the microheaters dissipates to the graphene primarily through the graphite, the latter being a good thermal conductor as a metal [7]. A thinner hBN flake minimizes the vertical path between the gold and graphite, facilitating the heat transfer to the graphite. This point will be discussed in Section 3.2. Lastly, in addition to fully encapsulating the graphene, the bottom hBN should extend past the graphene-top hBN region and be large enough to accommodate the placement of the heaters, ideally on both sides of the graphene.

Graphite flakes

We look for elongated, homogeneous graphite flakes (Fig. 3.2d) that will serve as back-gate electrodes as well as a medium for heat dissipation to the graphene, as mentioned above. Along with the bottom hBN, graphite offers additional screening from the SiO_2 surface disorder and stronger capacitive coupling to the graphene [22]. Flakes thinner than ~4 layers are avoided as they might introduce unwanted effects due to the unique properties of few-layer graphene. Thicker flakes (> 5-7 nm) are also avoided because they are difficult to pick up. The flake should be long enough to be contacted without shorting to the graphene and to host the heaters. The narrow shape allows to have the graphene one-dimensional contacts extending outside of the local graphite gate, preventing shorting and enabling the independent gating of the Hall arms with the silicon gate.

3.1.3 Pick-up and stacking procedure

The stacks are made following a modified dry-transfer technique [17] which was optimized to mitigate challenges such as bubble formation [23], twist-angle disorder [24] and twist-angle

relaxation—at small twist angles, spontaneous lattice relaxation effects tend to enlarge the AB/BA regions at the expense of the AA regions, as AB/BA stacking is energetically more favorable [25]—. This subsection presents the stacking setup, key preparatory steps for a successful stack and a description of the stacking process.

Transfer stage

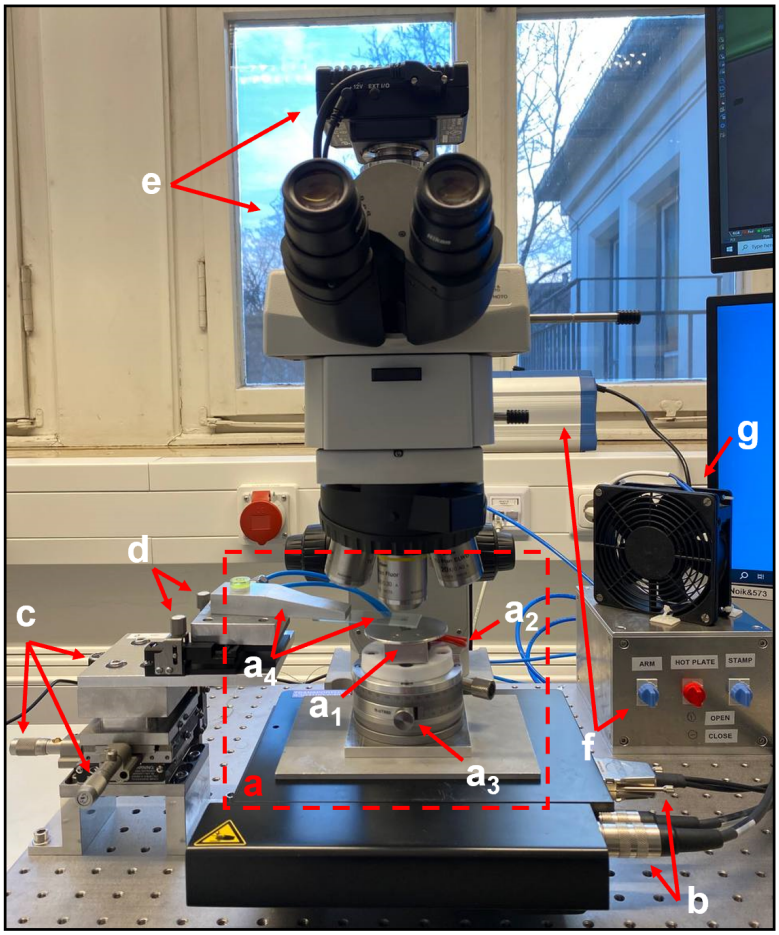

Figure 3.3: Transfer stage for flake search, pick-up and stacking. The main components of the setup are a sample stage (**a**, **b**), a micromanipulator stage (**c**, **d**) and a microscope (**e**). The individual components are described in the text.

The home-built transfer stage comprises several components mounted on an optical breadboard that features broadband vibration damping. It is used for flake search and identification, graphene-cutting and stacking. In the following, the individual components shown in Fig. 3.3 are described.

The central part of the setup **(a)** consists of a top plate **(a_1)** with a small hole in the middle where the substrate containing the flakes is placed and secured by vacuum. It also houses a heating element and a thermocouple **(a_2)** for temperature control during stacking. The plate is mounted on a manual rotation stage **(a_3)** equipped with a vernier

scale that enables angular measurements of 0.017° precision, which is used to achieve the twist angle of ~1.1°. The rotation stage is separated from the top plate by a Teflon disk, ensuring thermal isolation and stability. The assembled elements are mounted on a motorized XY sample stage **(b)**, allowing precise alignment of the flakes. The stamp **($\mathbf{a_4}$)** used for pick-up and stacking is held through vacuum by a metallic arm that can be positioned in x, y and z using a micromanipulator **(c)**, which controls the motion of the stamp. With a second micromanipulator **(d)**, the tilt angle of the stamp can be adjusted, enabling controlled contact between the stamp and the chip (see next segment).
The microscope **(e)** allows for seamless switching between the binoculars and the camera. The binoculars are rather used for faster flake search as they offer a wider field of view. For stacking, we look at the image acquired by the camera, paired with an imaging software with tools such as alignment marks and LUTs. Long-distance objectives are employed for focusing the stamp and the flakes while providing enough clearance for the vertical motion of the stamp. In order to properly focus the desired regions through the glass slide that hosts the PDMS/PC stamp, we close the aperture diaphragm of the microscope, minimizing the amount of scattered light from the glass and increasing the contrast.
The metallic arm, stamp and chip are kept in place during stacking through a vacuum pump connected to three valves **(f)**, allowing the vacuum to be separately turned on and off for each component. Finally, a fan **(g)** is installed in order to accelerate the cool-down of the hot plate when needed.

Pick-up using a PDMS/PC stamp

The stamp consists of a thin polycarbonate (PC) film attached to the surface of a small polydimethylsiloxane (PDMS) block mounted on a glass slide, as shown in Fig. 3.4a. The PC serves as an adhesion layer that bonds strongly to hBN, allowing its pick-up from the silicon dioxide substrate. Conversely, graphene adheres more strongly to the SiO_2 and cannot be directly picked up by the PC. Instead, it is picked up by a top hBN flake at temperatures around 100 °C. This is possible thanks to the high glass transition temperature of PC of T_g ~150 °C, which enables stacking at higher temperatures of 100-120 °C, facilitating pick-up and enhancing bubble mobility [23]. The PDMS acts as a viscoelastic support to the PC that allows controlled and uniform contact to the flakes.

- **Stamp preparation**. The stamp is prepared similar to [26]. The PC film is made from a solution of PC pellets dissolved in chloroform at a 6 % weight concentration. After pipetting a few drops of the PC solution on a clean glass slide, we immediately put a second, clean glass slide on top of the first one and slide the two over each other such that we obtain a flat, homogeneous film with few or no wrinkles on both slides. To improve film homogeneity, the PC is baked at 150 °C for ~1-2 min. The

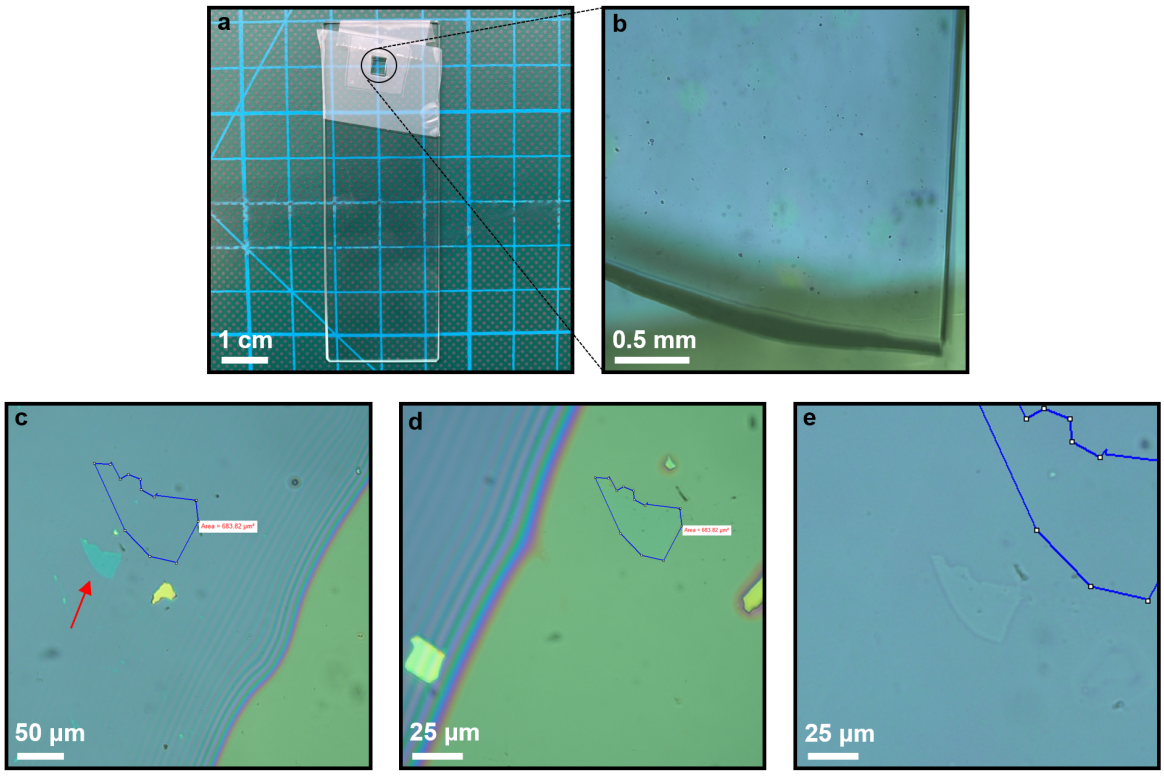

Figure 3.4: PC on PDMS stamp for pick-up and stacking. a, Stamp made of a PC film attached to a PDMS block mounted on a glass slide. **b**, PC film under the optical microscope, featuring clean areas and contaminated regions (black spots). **c-e**, Pick-up of an hBN flake at 100 °C. The stamp is gradually lowered to controllably approach the hBN flake from the corner of the stamp (**c**) until the wavefront fully propagates over the flake (**d**). The stamp is then slowly retracted and the "shadow" in the retracted stamp indicates a successful pick-up (**e**).

film is then cut in ~1x1 cm^2 pieces that can be used for the stamp.
To assemble the stamp, we take a small piece ~2x2 mm^2 of commercially available PDMS and place it on a clean glass slide. The PDMS is pre-cleaned with ozone to enhance the adhesion of the PC film to the PDMS surface. A piece of scotch tape with a small window slightly larger than the PDMS is used to pick up the PC film from the glass slide and place it on the PDMS. Finally, the assembled stamp is baked at 105 °C for 5 min to further enhance the adhesion of the PC.
Note that while the ozone pre-treatment prevents the detachment of the PC from the PDMS during the pick-up of the flakes, the PC might not be able to detach properly from the PDMS when releasing the stack on the pre-patterned chip. This also depends on the prepared PC solution and the thickness of the PC film. Therefore, we carefully prepare a few stamps and test them to select the best ones.

- **Pick-up.** Fig. 3.4b shows a region of the PC stamp under the optical microscope. It is important to choose a clean area free of visible contaminants where the flakes will

be picked up. To controllably approach and pick up the flakes, we tilt the stamp at an appropriate angle relative to the chip using the micromanipulator. This ensures that initial contact occurs between a corner of the stamp and a region of the chip reasonably far from the target flake, preventing sudden contact to the flake that might cause it to tear or fold. Fig. 3.4c-d demonstrates the successful pick-up of an hBN flake at ~100 °C. First, the stamp is gradually lowered with the z-micromanipulator until it touches the chip at the desired point. As contact is established, a green color surrounded by Newton's rings becomes visible, which we refer to as a "wavefront". The stamp is then further lowered until the wavefront fully propagates over the flake, after which it is retracted. The motion of the wavefront should be as smooth as possible to avoid damaging the flake. If the pick-up is successful, one can see the "shadow" of the flake on the fully retracted stamp.

Graphene-cutting using an AFM cantilever

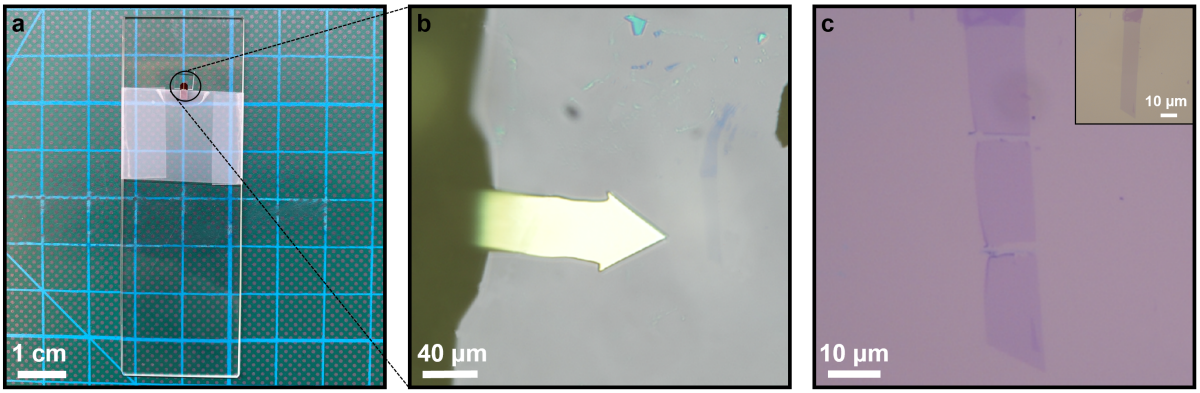

Figure 3.5: AFM cantilever for graphene-cutting. **a**, AFM cantilever placed on the edge of a PDMS block mounted on a glass slide. **b**, AFM tip in contact with the substrate containing the target graphene flake. **c**, Graphene flake with clean cuts carried out using the AFM tip. The inset shows the flake before cutting.

The two graphene sheets used to create a twisted bilayer originate from a single exfoliated graphene flake which is cut in two roughly equal parts. This guarantees that both sheets share the same crystal orientation prior to twisting, such that the imposed twist angle of ~1.1° is accurate.

The cut is done with an AFM cantilever placed on the edge of a small piece of PDMS at ~45° angle, mounted on a glass slide (Fig. 3.5a). Using the micromanipulators, the AFM tip is lowered to a position near the target flake until it touches the substrate. Upon contact, the AFM tip bends slightly causing a change in its reflectance, which manifests as a color shift from black to yellow (Fig. 3.5b). At this point, the sample stage is horizontally moved in a fast manner such that the flake goes below the AFM tip, resulting in a clean

cut (Fig. 3.5c).
This cutting method is fast, efficient and can be done directly at the transfer stage. Occasionally, the AFM tip might cause rips in the graphene sheet due to the nature of the process. This can be avoided by placing the AFM tip at an appropriate angle relative to the PDMS piece as well as identifying the optimal point of contact between the tip and the substrate before moving the flake over the tip: not too low as to break the tip, but not too high as to cause an incomplete or poor cut.

Stack conception

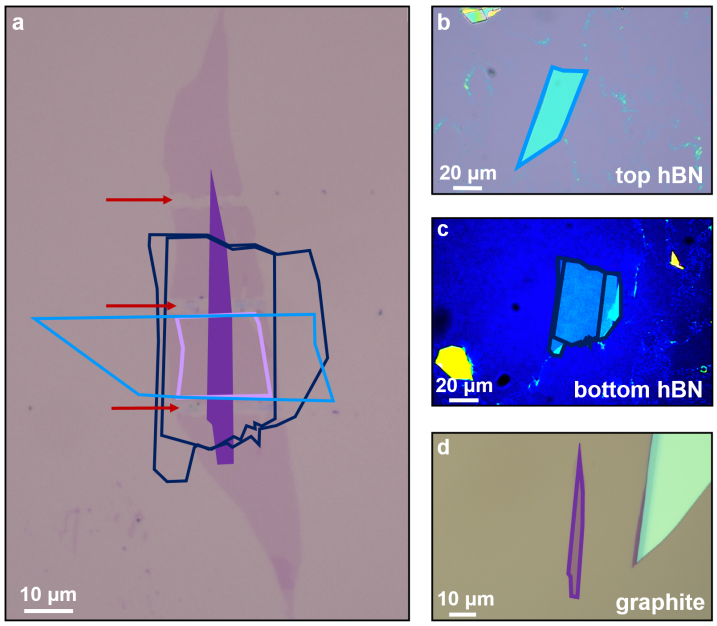

Figure 3.6: Plan of a twisted bilayer graphene stack. The conceptual alignment and orientation of the flakes relative to each other is done starting from the graphene flake (**a**). The red arrows indicate the cuts carried out with an AFM tip to make two separated graphene sheets that fit inside the top hBN. The top hBN (**b**) is positioned such that its two sharp edges roughly align with the edges of the graphene sheets (the second graphene sheet is outlined in light violet). The homogeneous part of the bottom hBN (**c**) is marked by a rectangular outline within the full flake and is placed such that it encapsulates the graphene and forms a region of only bottom hBN and graphite back-gate (**d**) on both sides of the graphene edges, which is intended for placing the microheaters.

In the remainder of this subsection, we demonstrate the stacking procedure using the twisted bilayer graphene sample that led to a thermopower device with a 0.99° twisted region. The preparation of single-layer graphene samples follows the same steps, omitting those related to twisting.

Before proceeding to the actual stacking, we first conceptualize the stack by selecting compatible flakes and planning their arrangement to achieve our desired geometry. Following

up on the flake selection, we choose a graphene flake from which we cut two roughly equal sheets such that each sheet fits almost exactly inside the top hBN, as illusrated in Fig. 3.6. The graphite and the bottom hBN flakes are then oriented to form a graphite-bottom hBN-only region on both sides of the graphene, where the gold microheaters will be placed. Additionally, aligning the graphite flake such that it is fully covered by the bottom hBN reduces the strain introduced during the pick-up of the graphite, minimizing twist angle relaxation. However, this step could not be achieved in this particular stack.
Since the orientation of the stamp is fixed during stacking, the orientation in which the first flake (top hBN) is picked up determines the orientation in which the rest of the flakes will be picked up. Sometimes, it is important to choose a convenient orientation to avoid pick-up from a side which has a thick flake close to the target flake (as in Fig. 3.6d), or from a side in which the target flake is prone to tearing when retracting the stamp (for example a side in which the flake has a small initial tear that might propagate when retracting the stamp). While we prioritize selecting flakes that do not present these issues, the availability of such flakes highly depends on the exfoliation yield considering all criteria at the same time. Nevertheless, with careful planning and precise stacking a successful stack can be achieved.

Stacking process

With all necessary elements ready, we can proceed to the stacking process, which is illustrated in Fig. 3.7 and goes as follows:

- **Graphene cutting and top hBN pick-up**. After cutting the graphene flake with the AFM cantilever (Fig. 3.7a), we proceed to picking up the top hBN at 100 °C with the PC stamp (Fig. 3.7b), as explained in the pick-up segment. The motion of the wavefront can be controlled either mechanically via the the z-micromanipulator or thermally by changing the temperature while keeping the stamp fixed: ramping up the temperature causes thermal expansion of the PC such that the wavefront advances, while decreasing it back causes the wavefront to recede. We opt for the way that looks smoother on the flake at the time of the specific pick-up.

- **Alignment and pick-up of the first graphene sheet**. Using precise positioning of the XY sample stage, the first graphene sheet is aligned with the edges of the picked-up top hBN to achieve the so-called “clamping” (Fig. 3.7c), where the edge of the graphene effectively folds over the edge of the hBN, restricting the motion of the graphene and therefore reducing the chance of twist angle distortion and relaxation. Note that the cut edge of the graphene offers an even better clamping point due to its increased roughness. To avoid an additional Moiré potential arising from graphene-hBN alignment [27], which we don’t aim to study in this thesis, we

make sure that there is a small misalignment between the graphene and hBN edges. In this stack, the graphene could only be clamped from one side (see red arrow in Fig. 3.7c), when it could have been clamped from the top edge as well. This was due to the fact that the graphene flake was cut slightly too small for this to be possible.

- **Second graphene sheet**. After properly aligning the second graphene sheet such that it also clamps to the hBN, it is rotated by ~1.1° using the vernier scale of the rotation stage, after which it is picked up (Fig. 3.7d). To prevent any additional, unintentional rotation, the stamp is moved solely in the z-direction between the first and second graphene pick-up.

- **Pick-up of the bottom hBN and graphite back-gate.** Following the pick-up of the bottom hBN (Fig. 3.7e), the graphite gate is picked up through thermal expansion and retraction of the wavefront by ramping the temperature up then down between 100 °C and 110 °C (Fig. 3.7f-g). This has been shown to push most of the bubbles out of the device area due their higher diffusivity at higher temperatures.

- **Stack deposition on a pre-patterned electrode chip.** Having successfully picked up all the flakes, the next and final step is to drop the stack onto an Si/SiO_2 substrate where gold electrodes have been evaporated (Fig. 3.11j). Prior to dropping, the pre-patterned chip is sonicated with acetone, isopropanol and deionized water, in addition to oxygen plasma treatment to improve the adhesion of the stack to the chip. The stack deposition goes as follows: starting from a temperature of 120 °C, the stamp is positioned such that the stack falls on the center of the chip, after which it is gradually lowered until the wavefront propagates fully over the stack. The wavefront is moved a further ~200 µm beyond the stack to prevent sudden detachment of the PC from the PDMS near the stack. At this point, the temperature is increased from 120 °C to 180 °C. During this phase, the stamp is slightly moved up whenever Newton's rings reappear to stop further propagation of the wavefront. When the glass transition temperature of the PC is reached at approximately 150 °C, the PC starts detaching from the PDMS. At T ~180 °C, the PC fully melts and the stamp can be retracted completely, securely leaving the stack on the chip (Fig. 3.7h).
  The PC is washed off by immersing the chip in chloroform for a few minutes followed by rinsing in acetone and isopropanol, then blow-drying with nitrogen. The stack (Fig. 3.7i) is now ready for fabrication into a measurable device.

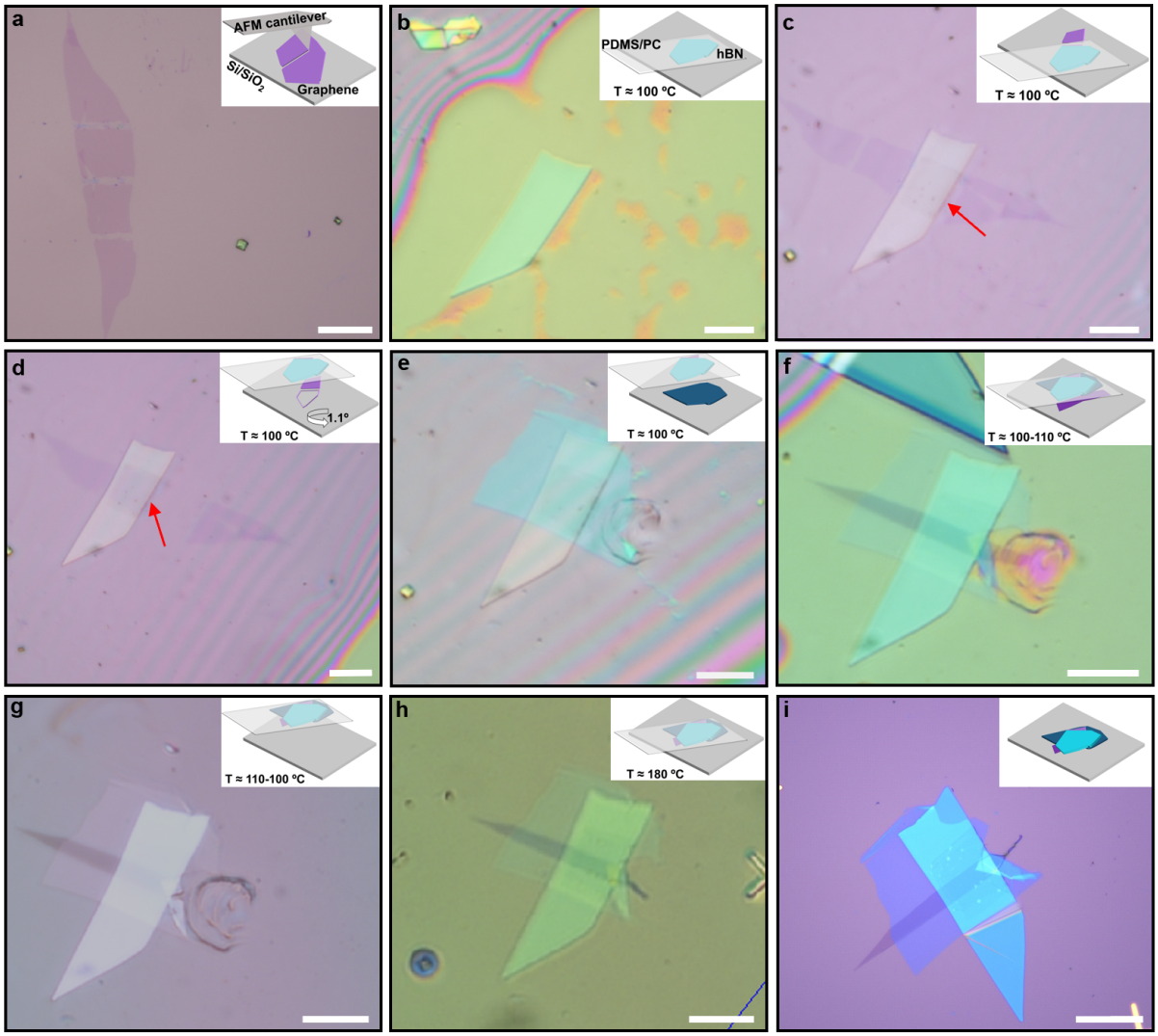

Figure 3.7: Stacking of a twisted bilayer graphene sample. **a**, The graphene flake is cut into two roughly equal sheets using an AFM cantilever. **b**, The top hBN flake is picked up with the PC stamp. The observed orange spots are unusual and might be due to increased humidity at the time of the stack. **c**, The first graphene sheet is picked up after it has been aligned such that its edge clamps to the edge of the hBN flake, indicated by the red arrow. **d**, The second graphene sheet is aligned similar to the first one then rotated by ~1.1° and picked up. **e**, Alignment and pick-up of the bottom hBN flake. We notice that after step (**d**), a region of the stamp has been deformed, but it was still possible to finish the stack without damage to the device area. **f-g**, Alignment and pick-up of the graphite gate via thermal expansion (**f**) and retraction (**g**) of the wavefront at high temperatures. This process allows to effectively push out bubbles outside the device area. **h**, The stack is released from the PC stamp onto an Si/SiO_2 chip with pre-patterned electrodes. **i**, Optical image of the final stack after washing off the PC with chloroform. The scale bar is 20 µm.

3.2 Design and fabrication of graphene devices for thermoelectric measurements

3.2.1 Device geometry

Hall bar

We design a standard Hall bar to measure both the longitudinal and transverse response in electrical (Fig. 4.1) and thermoelectric (Fig. 3.12) transport. For the TBG device, we performed an AFM scan (Fig. 3.8) to identify regions visibly free of bubbles, and carefully positioned the Hall arms within those areas. For the SLG test devices, we initially designed 1 µm wide Hall arms spaced equally by 1 µm, typically used in our group. However, to attempt a temperature calibration at low temperatures—using temperature-dependent features such as quantum Hall plateaus in SLG or correlated states in TBG—we modified the design for the TBG device. There, we implemented 0.5 µm wide pairs of arms, with 0.5 µm spacing within each pair and 1.5 µm distance between each pair of arms (see D4 in Fig. 3.9). This geometry allows to assign a local temperature at each region of the device spanned by the pair of arms, and then the temperature difference between them, as elaborated in Section 5.1.

Heater placement and dimensions

To generate a temperature gradient along the device, gold microheaters were placed in proximity to the sample, with dimensions (width, length, thickness)

$$W = 300\,\text{nm},\ L = 6 \text{ to } 10\,\mu\text{m},\ t = 55\,\text{nm}.$$

From the four-probe electrical resistance of the heaters, we find a heater resistance R_h in the order of 15-30 Ω at 300 mK (Fig. 3.10). This value is quite low compared to the 1 kΩ achieved in [7], where they used a similar width but a much lower thickness of 8 nm. Still, our dimensions showed to be sufficient to measure thermovoltage at low temperature by sending heater currents between 5 µA and 60 µA, which corresponds to a power of 1-100 nW. One possible optimization step in this project to achieve sufficient heating power with a lower current (e.g. hundreds of nanoamps) would be to narrow/thin down the heaters and test them in terms of stability.

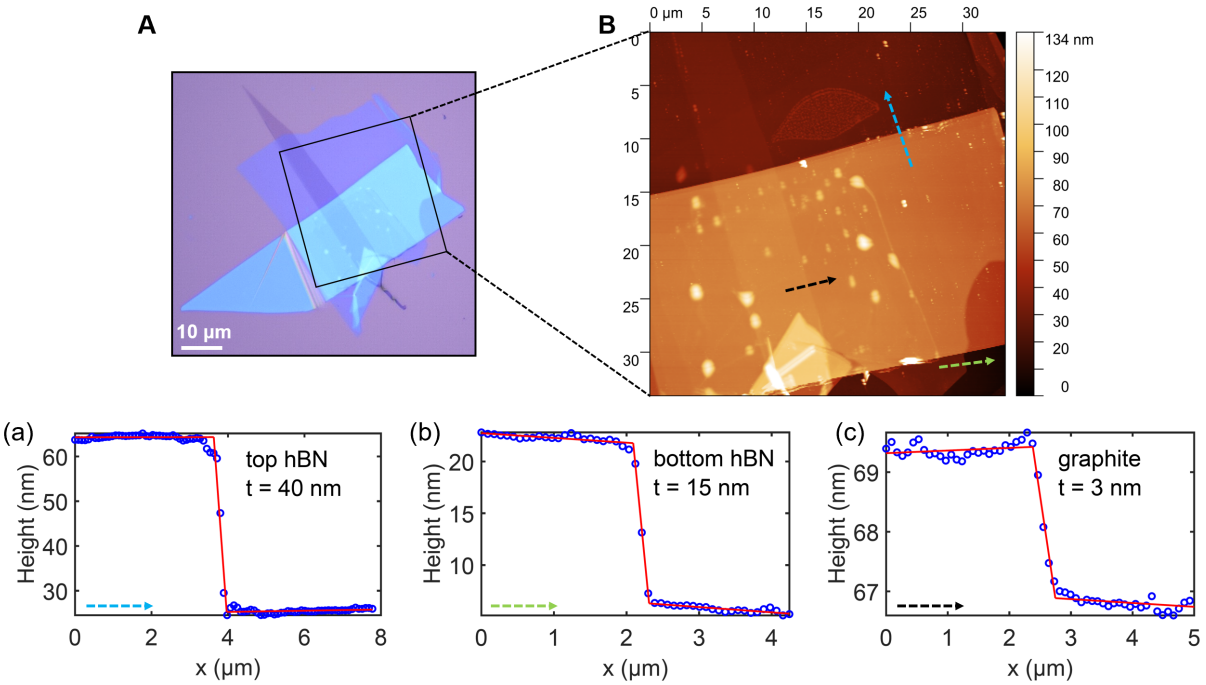

Figure 3.8: AFM characterization of the TBG stack. **A**, Optical image of the hBN/TBG/hBN/graphite stack. **B**, AFM scan of the stack region outlined in **A**. This image allows the identification of regions with the least bubbles where the Hall bar will be fabricated. **a-c**, Height profiles along the lines indicated by arrows in **B**, from which the layer thicknesses are extracted. In this stack, we find that the top hBN (**a**) is rather thick (40 nm). The thicknesses of the bottom hBN (**b**) and graphite (**c**) are 15 nm and 3 nm respectively.

We tested various heater placements on the stack: on SiO_2, top hBN, and bottom hBN-graphite (see cross-sectional schematic in Fig. 3.12). Placing the heater on the bottom hBN-graphite region, in contrast to the SiO_2 region typically used in such experiments on graphene [5, 14], required thorough flake selection and stacking, and was motivated by the higher thermal conductivity of graphite as opposed to SiO_2 at ultralow temperatures, which helps establish a more uniform temperature gradient while avoiding the poor thermal path through the SiO_2 [7]. Although our data does not provide a definite conclusion as to which placement provides a better temperature gradient, our measurements on the SLG devices at 40 K suggest that the bottom hBN-graphite heater performed better than the SiO_2 heater (see Fig. 3.13), despite both having identical dimensions and being placed the same distance from the measured probes, with the same heater current applied. A similar comparison in the TBG device is shown in Fig. 5.10 at 40 mK, where the SiO_2 heater appeared to introduce more disturbance to the signal compared to the bottom hBN-graphite heater, while both provided signals of similar magnitude. However, further investigation is necessary to understand whether this effect is device-dependent. We further note that in device D2, where the bottom hBN is rather thin (Fig. 3.9D2), the heater

placed on bottom hBN-graphite broke at the edge between the graphite and the hBN after cool-down to 300 mK, likely due to the different thermal expansion rates of the two materials. This suggests that very thin hBN flakes should be avoided in future designs.

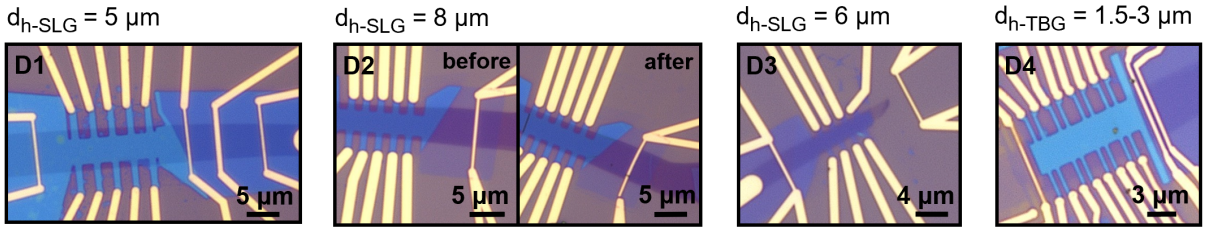

Figure 3.9: Device catalog for thermoelectric measurements. D1-D3, Single-layer graphene test devices with gold microheaters placed on different regions of the stack to test their efficiency. For D2, the left image shows the device before measurement in a cryostat and the right image is after unloading. **D4**, Working twisted bilayer graphene device used for the main measurements. The sample-to-heater distance for each device is given on top of each panel.

All in all, we demonstrate in Section 5.1 that the heater on bottom hBN-graphite provides a reliable measurement scheme, and the same procedure can be repeated for the SiO_2 heater to gain further insights. The temperature calibration on the latter was not possible within the time frame of this thesis. In the remainder of this thesis, we present and discuss the results obtained on the TBG device, where the heaters were placed as close as possible to the sample, with a sample-to-heater distance of 1.5 µm for the heater on SiO_2 and 3 µm for the heater on bottom hBN-graphite.

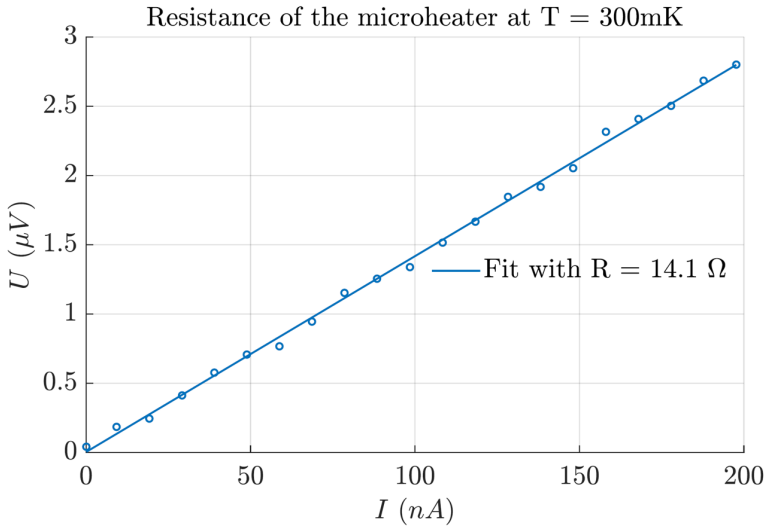

Figure 3.10: Resistance of the gold microheater. Four-probe voltage U vs current I curve at $T = 300$ mK for the gold microheater with dimensions $W = 300$ nm, $L = 6$ µm and $t = 55$ nm. The extracted resistance is $R_h = 14.1\,\Omega$.

3.2.2 Nanofabrication process

The device geometry is defined with the KLayout software [28] and implemented in three lithography steps, described in Fig. 3.11. The patterns are written using electron-beam lithography, where a focused beam of electrons selectively exposes a resist material, enabling the definition of nanoscale features with precise control over pattern placement and dimensions. The Hall bar is etched through reactive ion etching (RIE), a dry-etching technique that utilizes plasma [29] to selectively remove the exposed material. In this step, the heterostructure is etched until the material between the graphene probes is completely removed, forming the Hall bar shape (Fig. 3.11d). For contacting the graphene to the pre-patterned gold pads, the written contacts are etched with a well-calibrated etching rate to create a proper 1D edge contact between the gold and the graphene [30]. Improper etching, whether over- or under-etching, can lead to high-resistance contacts or result in a complete failure to establish contact, making the device unusable. Chromium and gold are then deposited using an ultra-high vacuum e-beam evaporator, with chromium serving as an adhesion layer. To remove unwanted metal, the chip is submerged in hot acetone (50 °C), where the acetone dissolves the resist, lifting off the metal on top of it and leaving behind the gold only in the exposed contact areas (Fig. 3.11g). Lastly, the gold microheaters are similarly defined with electron-beam lithography, evaporated without etching and lifted off, completing the fabrication process (Fig. 3.11i).

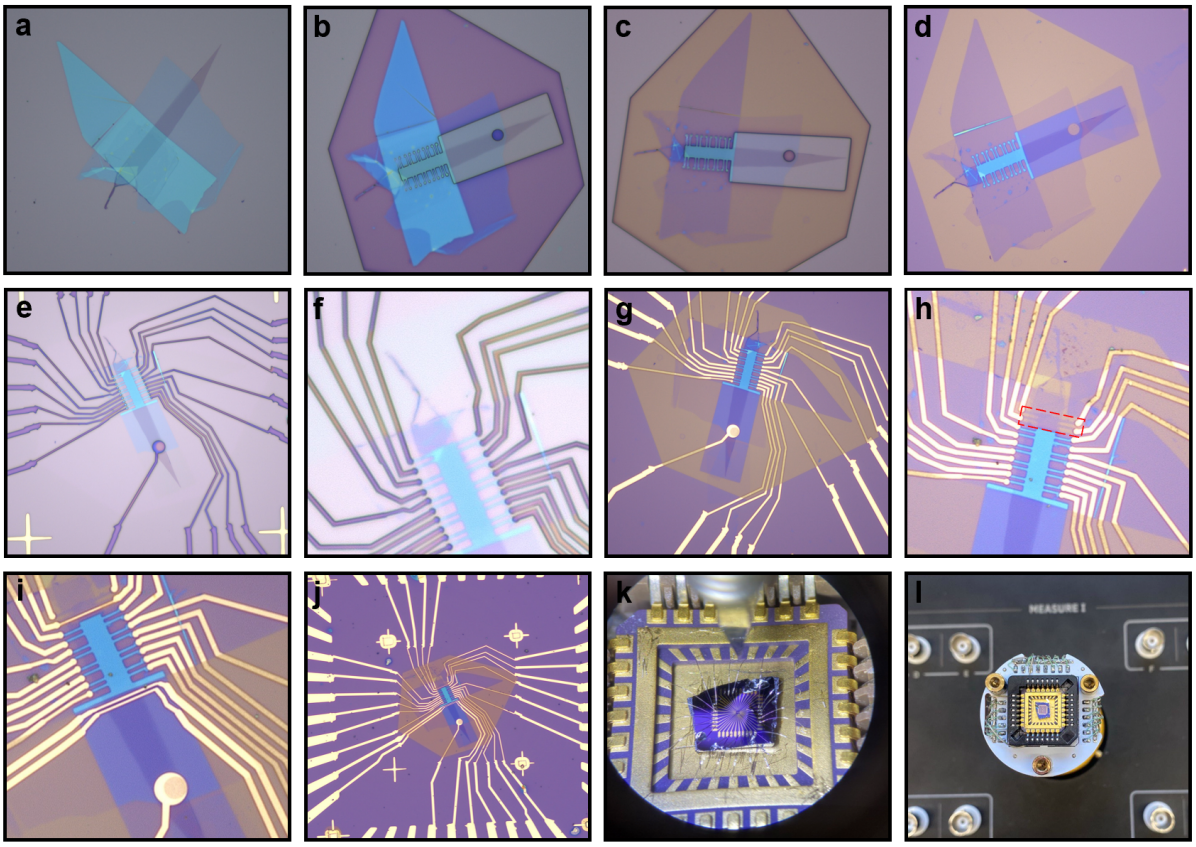

Figure 3.11: Device fabrication steps. **a-d**, Etching of the Hall bar. After spin-coating the e-beam resist (PMMA) on the stack (**a**), the sample is exposed using an electron beam lithography system and developed in a 1:3 MIBK:IPA solution to define the Hall bar shape (**b**). The exposed area is then etched away (**c**) and the resist is rinsed with acetone and IPA, leaving behind the Hall bar structure (**d**). **e-g**, Evaporation of the contacts. In this fabrication step, the contacts are once again exposed using e-beam lithography (**e**), followed by etching to form 1D edge contacts to the graphene, as well as to open a window through the bottom hBN, exposing the underlying graphite for electrical connection (**f**). After e-beam evaporation of 5:50 nm chromium:gold, the lift-off process removes the gold from the unexposed areas, thereby completing the contact formation (**g**). **h**, Additional etching of a sample area (outlined in red) that caused a gate leak in the device. **i**, Similar to the contacts, the gold microheaters are defined and directly deposited on a stack region and/or the SiO_2 without etching, marking the final step of the fabrication process. **j**, Zoomed-out view of the final device. **k**, The Si/SiO_2 chip with the device is secured on a chip carrier using conductive silver paste, then wire-bonded for loading into a cryostat/fridge. **l**, Wire-bonded device placed on the cryostat's sample holder, ready for loading and measurement.

3.3 2ω lock-in technique for thermoelectric measurements

The measurements are performed using standard lock-in detection, where the device is driven by a low-frequency AC signal at frequency ω (reference signal), and its response is measured using a lock-in amplifier (Stanford Research SR860 in our case). The detected input signal contains both the desired response—typically appearing at harmonics of ω, depending on the underlying physical mechanism—and broadband noise such as line frequency pickup and random fluctuations. To extract the signal of interest from the noise, the lock-in performs dual-phase demodulation: the input is multiplied by the reference signal and its 90°-phase-shifted counterpart, followed by low-pass filtering to isolate the narrow-band response [31]. The resulting outputs are two channels X and Y, referred to as in-phase ($\Theta = 0$) and quadrature components ($\Theta = 90°$), where Θ is the phase difference between the reference signal and the output signal. The magnitude and phase of the response can then be obtained from

$$R = \sqrt{X^2 + Y^2}, \ \Theta = \text{atan2}\,(Y, X). \tag{3.1}$$

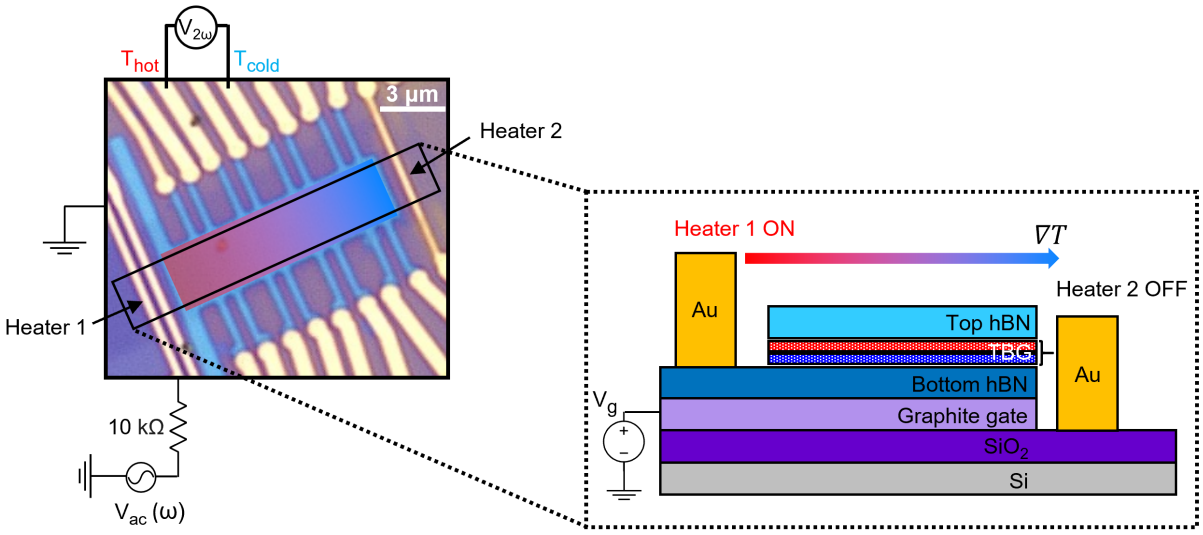

Figure 3.12: Thermoelectric transport measurement scheme. Sending a low-frequency AC current through the heater ($I_h(\omega) = 10\,\text{k}\Omega \cdot V_{ac}(\omega)$) induces a temperature gradient along the length of the device via Joule heating, generating a longitudinal thermoelectric voltage between two regions of the device, where T_{hot} is the closer region to the heater and T_{cold} is the farther one. This voltage is collected at double the frequency of the heating power with a lock-in amplifier ($V_{2\omega}$). The dependence of thermovoltage on carrier density is investigated by sweeping the graphite gate voltage.

In our measurement scheme, the driving signal is the current $I_h(\omega)$ sent through the

gold microheater, which heats it via Joule heating with power $P_{Joule} = R_h I_h^2$. This heat dissipates from the heater through the stack and substrate, inducing a temperature gradient $\boldsymbol{\nabla} T$ along the length of the device (Fig. 3.12) and resulting in a temperature difference ΔT between two contacts. This in turn induces a thermoelectric voltage between the contacts, which can be measured as the second harmonic Y-component of the lock-in. This measurement technique is known as the 2ω lock-in technique and has been widely used in previous studies of thermoelectricity in 2D materials [5, 7]. The measured thermovoltage $V_{th} \propto \Delta T \propto P_{Joule}$ oscillates at double the frequency of 2ω due to the quadratic dependence of the Joule power on heater current: for $I_h = I_0 \cos(\omega t)$,

$$\begin{aligned} P_{Joule} &= P_0 \cos^2(\omega t) \\ &= \frac{P_0}{2} + \frac{P_0}{2} \cos(2\omega t). \\ &= P_{DC} + P_{2\omega} \end{aligned} \tag{3.2}$$

The detected signal by the lock-in only "sees" the oscillating component, such that

$$V_{th} = V_{2\omega} = V_0 \cos(2\omega t + \Theta). \tag{3.3}$$

In the context of measuring the Seebeck coefficient, both the amplitude and the sign of the thermoelectric voltage are of paramount importance. The sign, in particular, provides critical information about the type of charge carriers (electrons or holes) when tuning the carrier density, which is essential for understanding the underlying transport mechanisms, especially in MATBG. In a first-order approximation, the real system can be seen as a thermal RC circuit with thermal capacitance C_{th} and thermal resistance R_{th}, where the phase shift between the heating power and the induced temperature difference approaches $\Theta = 90°$ for low frequencies $\omega \ll \omega_{\text{cut-off}} = (R_{th} C_{th})^{-1}$. This is similar to an electrical RC circuit, where the voltage across the capacitor (analog to ΔT) lags the current (analog to P_{Joule}) by 90° at low frequencies. Therefore, the thermoelectric response, measured as the second harmonic voltage, is expected to appear predominantly in the Y-channel of the lock-in in an ideal measurement scheme, making the interpretation of the Seebeck signal more straightforward in terms of both amplitude and sign. For the single-layer graphene devices, a signal was detected in both the X and Y channels when using $f = \omega/2\pi = 13\,\text{Hz}$ (Fig. 3.13A). Further investigation of the frequency dependence of the signal was only conducted for the twisted bilayer graphene device, where a stable phase of ±90° was achieved at $f = 3\,\text{Hz}$ (Fig. 5.7).

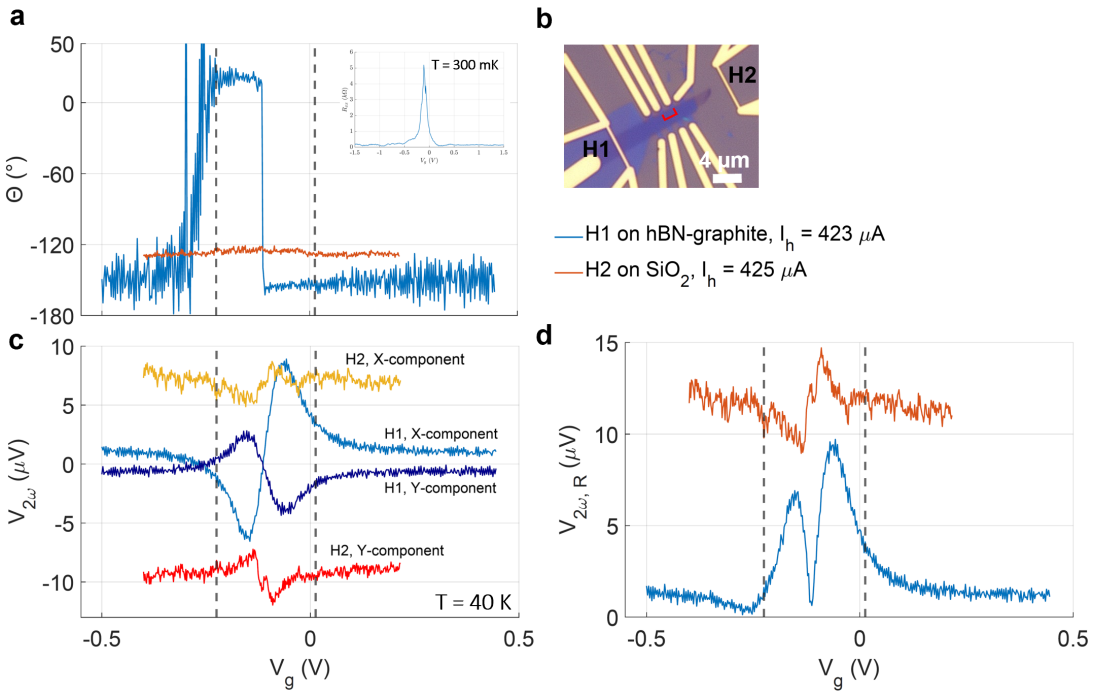

Figure 3.13: Lock-in components of the thermoelectric signal in an SLG device at $T = 40\,\mathrm{K}$. **a**, Phase of the measured second harmonic voltage $V_{2\omega}$ with $f = 13\,\mathrm{Hz}$ using one heater at a time, as labeled in panel **b**. For heater H1, the phase jumps from $+15°$ to $-150°$, indicating a change in carrier type from holes to electrons across the Dirac point, as expected for single-layer graphene. The inset shows R_{xx} vs. gate voltage at 300 mK, where the Dirac peak appears at the same gate voltage as the phase jump. The most stable phase is observed within the outlined gate voltage range. **b** Optical image of the device, with the measured contact pairs indicated in red. **c** X and Y components of the lock-in signal for each heater. For H1, the signal shows a more consistent behavior with the expected thermovoltage. **d** Comparison of the magnitude $V_{2\omega,R}$ for the two heaters. A larger magnitude is observed for the graphite–hBN heater, while an offset is seen for the SiO_2 heater.

4 Electrical transport characterization

For a better understanding of the thermoelectric measurement results, we first conduct low-temperature magnetoelectric transport measurements to identify the existing electronic states in the devices. After introducing the measurement scheme and the expected electrical resistance response, we determine the twist angle of the twisted bilayer graphene device, assess its homogeneity and identify key electronic states for comparison with the thermoelectric measurements.

4.1 Resistance signatures of the (MA)TBG band structure

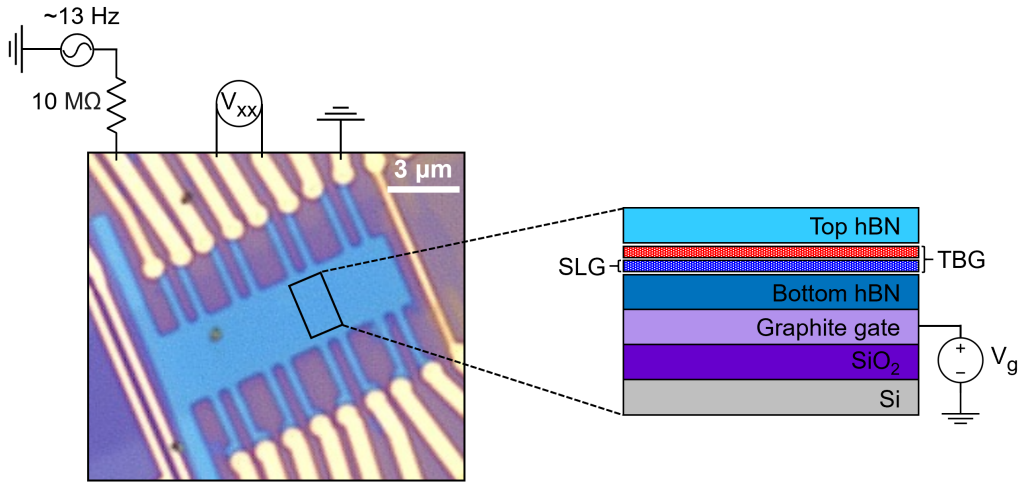

Figure 4.1: Electrical transport measurement scheme. The four-probe resistance $R_{xx} = \frac{V_{xx}}{I}$ of a device region is measured by applying a low frequency AC voltage (~100 mV) through a resistor of 10 MΩ such that a small AC current (I ~10 nA) flows between the source and drain contacts. The voltage drop V_{xx} across inner probes is then measured with a lock-in amplifier. The graphite layer acts as capacitor plate that allows electrostatic gating of the graphene layers when applying a DC voltage to the graphite back-gate electrode.

We employ the lock-in technique described in Section 3.3 to measure the four-probe resistance by sending a small, low frequency AC current between the source and drain contacts and measuring the voltage drop across the inner probes, as illustrated in Fig. 4.1. The resistance response exhibits a strong carrier density dependence, enabling the exploration of various electronic states within a single device [32]. The carrier density is tuned by electrostatic gating via the graphite back-gate, which induces charges in the TBG layer,

effectively shifting the Fermi level within the band structure of the material.

In magic-angle twisted bilayer graphene, a series of resistance peaks are observed at integer fillings of the flat band, separated by low-resistance metallic states [32], as shown in Fig. 4.4. The peak at the charge neutrality point (CNP) and those at full-filling are well explained by the non-interacting band structure, where the latter correspond to insulating states arising from interlayer hybridization [33], with a measured thermal activation gap of tens of meV [2, 33]. This gap can be understood as the gap between the flat band and the far dispersive bands, and is referred to as the "superlattice gap" or the "band insulator" (BI). In contrast, peaks observed at lower integer fillings cannot be explained in the absence of electron-electron interactions and are interpreted as correlated insulators (CI): within the flat band, the interaction energy U is much higher than the kinetic energy t, giving rise to interaction-driven energy gaps [2, 32]. In particular, the CI at half-filling has a much lower thermal activation gap compared to the superlattice gap (e.g. 0.3 meV in [2]), a property we will exploit to calibrate the temperature in the thermoelectric experiments (Chapter 5). For twist angles far from the magic-angle, only band insulators are observed, as the superlattice band remains rather dispersive to satisfy $U/t \gg 1$ [2].

4.2 Twisted bilayer graphene device

We begin by constructing a twist angle map across the device with an accuracy of $0.05-0.1°$ using the low-field Hall effect and acquired two-probe resistance traces. The twist angle of the region of interest for the thermoelectric experiments is then more precisely determined by tracing the quantized Landau levels emanating from the superlattice gap back to their origin, resulting in an accuracy of $0.01°$.

4.2.1 Twist angle map

The twist angle of the sample can be estimated from the superlattice carrier density through Eq. 2.29

$$n_s = \frac{4}{A_s} = \frac{8\theta^2}{\sqrt{3}a_0^2}, \quad \text{with} \sin^2(\theta/2) \approx (\theta/2)^2$$

where n_s is the gate-induced carrier density required to reach the superlattice gaps at full filling of the flat band. The factor 4 accounts for the spin and valley degeneracy coming from each layer. By performing magnetotransport measurements, the capacitance of the gate C_g can be accurately determined, allowing a conversion from applied gate voltage V_g

to a carrier density n centered around the Dirac point via:

$$n = \frac{C_g}{e} \cdot (V_g - V_D), \tag{4.1}$$

where V_D is the position of the Dirac point. With C_g known, the next task is to identify the position of the full filling $V_g(n_s)$, which is the main contribution to the uncertainty in the twist angle estimation, as will be discussed in this section.

Low-field Hall effect

Applying a perpendicular magnetic field gives rise to a transverse resistance R_{xy} across the Hall bar. In the low-field, classical Hall regime ($B < 1\,\mathrm{T}$), the Hall carrier density is given by [34]:

$$n_H = -\frac{B}{eR_{xy}}. \tag{4.2}$$

Near the charge neutrality point, it is expected that the only contribution to the Hall density comes from the gate-induced charge carriers n, being either electrons for positive gate voltages or holes for negative voltages, such that $n = n_H$ [2]. This is confirmed by the measurement shown in Fig. 4.2, where perfect linearity between n_H and V_g is observed around charge neutrality. Combining $\frac{\Delta n_H}{\Delta n} = 1$ with Eq. 4.1, we extract the gate capacitance from the slope $\frac{\Delta n_H}{\Delta V_g} = \frac{C_g}{e}$ of the linear fit, resulting in a value of $C_g = 344 \pm 2\,\mathrm{nF/cm^2}$.

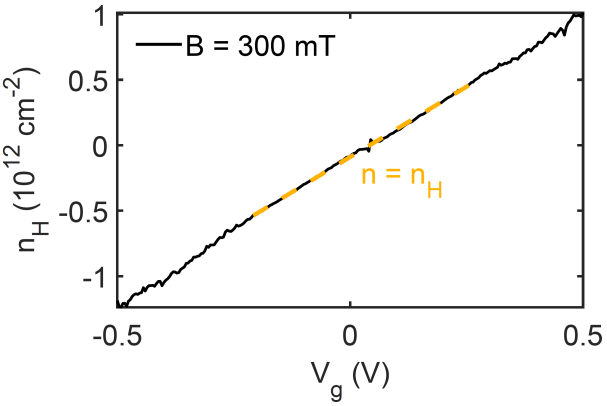

Figure 4.2: Hall density vs. gate voltage in the classical Hall regime. The measurement was done at $B = 300\,\mathrm{mT}$ and $T = 40\,\mathrm{mK}$. n_H was calculated from Eq. 4.2, where R_{xy} was antisymmetrized to correct for signal mixing between R_{xx} and R_{xy} due to geometric misalignment of the Hall arms: $R_{xy}^{antisymm.} = \frac{R_{xy}(B) - R_{xy}(-B)}{2}$.

Twist angle estimation

To construct the twist angle map across the device, we measure the two-probe resistance versus gate voltage for all pairs of arms and for each region, we identify the positions of the band insulators at full-filling $\nu = 1$ and the correlated insulators (if present) at half-filling

$\nu = 2$. The carrier density at those fillings is then given by:

$$\frac{n_s}{\nu} = \frac{C_g}{e} \cdot \left(V_g \left(\frac{n_s}{\nu} \right) - V_D \right).$$

Since the band insulators extend over a relatively wide range of V_g, their position is taken as the midpoint of that range. In this twist angle estimation, we also incorporate the positions of the correlated insulators when present. The final twist angle for each region is determined as the weighted average of the individual angles calculated from the positions of both the band and correlated insulators. This results in an error of $0.05 - 0.1°$ dominated by the uncertainty in the position of the fillings (see list of values in Table A.1).

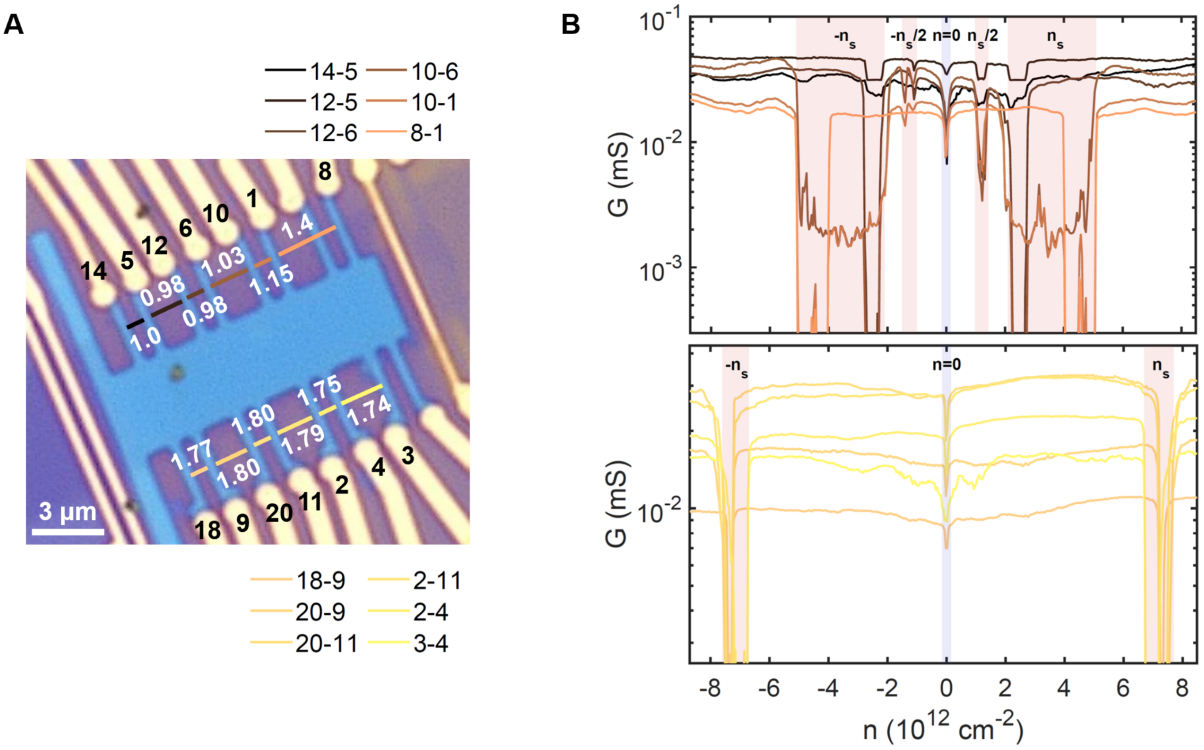

Figure 4.3: Twist angle map. **A**, Estimated twist angles for each region of the device. **B**, Two-probe conductance $G = R^{-1}$ vs. carrier density (calculated from Eq. 4.1) at $T = 40\,\text{mK}$ for the upper side of the device (upper panel) and lower side of the device (lower panel), plotted separately for clarity.

As can be seen in Fig. 4.3A, the upper side of the device (contacts 14 to 1) exhibits a twist angle ranging from 0.98° to 1.15°, which is close to the magic angle. The region between contacts 12 and 1 shows pronounced correlated insulator states at half-filling (Fig. 4.3B). Within this region, the position of the band insulator shifts as we move from contact 12 towards contact 1, indicating disorder and a gradual change in twist angle from lower to higher values. Since contacts 14 and 5 lie at the edge of the twisted area, the bands are expected to not be fully developed, which is reflected in the corresponding two-probe

trace.
If the peaks observed at $n \approx \pm 7 \times 10^{12}\,\mathrm{cm}^{-2}$ on the lower side of the device (contacts 18 to 3) correspond to band insulators, this would result in a larger twist angle of ~1.8°, far from the magic-angle. To rule out that the peaks do not arise from graphene-hBN alignment, further investigation is needed, such as examining the thermal activation behavior of the peaks.
This significant variation in twist angle across the width of the device is due to both the quality of the stack as well as the relatively large Hall bar width of ~3.5 µm. The quality of the stack aside, a narrower width of 1 to 2 µm could have resulted in a more homogeneous device, since twist angle disorder can be observed starting from ranges as small as 0.5 µm [24]. However, the trade-off is that the narrow device could have only captured the region with a larger twist angle, since it is initially unknown which region of the stack has the target twist angle. For the next generation of devices, the goal would be to improve stack quality and homogeneity, which can be achieved using the protocol described in Section 3.1 as demonstrated in the work by Jaime et al. [2], alongside the fabrication of narrower devices with a width of ~1 µm or lower.

4.2.2 Landau levels in the near-magic-angle region

To further characterize the device region exhibiting the correlated insulator states, we investigate the behavior of the corresponding four-probe resistance R_{xx} when the sample is subjected to a high perpendicular magnetic field, giving rise to Landau levels. From the analysis of the acquired Landau fan we once again extract the gate capacitance and twist angle.

Before proceeding further, we note that the four-probe resistance changes significantly depending on the source-drain configuration, as shown in Fig. 4.4. Specifically, the correlated insulator peaks are more pronounced when the source and drain contacts are closest to the probes. We attribute this behavior to the twist angle disorder discussed in the previous subsection, where the BI gap observed at around ±1 V corresponds to a region close to magic-angle and the one observed at around ±2 V corresponds to a higher angle. The Landau fan was acquired in the configuration where the correlated insulator peaks were less pronounced, as the measurement was conducted prior to this observation.

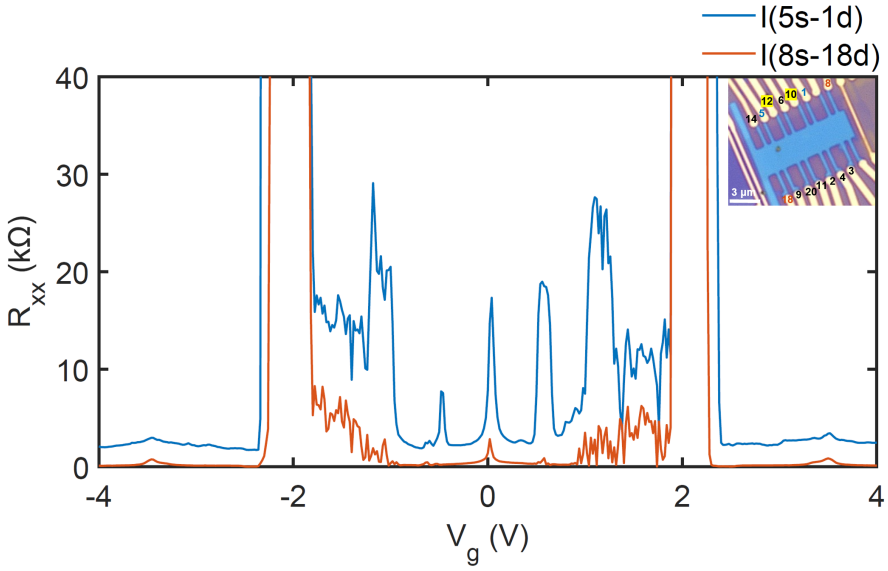

Figure 4.4: Longitudinal resistance vs. gate voltage for two different source-drain configurations. The measurement was performed at $T = 300\,\mathrm{mK}$ and $B = 0$. The inset shows the device image with the corresponding source (s)-drain (d) contacts and the probed region is highlighted in yellow.

Landau level quantization

Placing a two-dimensional electron system in a strong perpendicular magnetic field at low temperatures leads to the formation of Landau levels (LLs)—discrete energy levels resulting from the quantization of the cyclotron orbits of the charge carriers. For graphene, the energy levels are given by

$$E_N = \mathrm{sgn}(N)\sqrt{2\hbar v_F^2 eB|N|}, \tag{4.3}$$

where N is a positive integer for electrons and negative for holes, whereas the $N = 0$ Landau level is shared equally between both carrier types [35]. Single-layer graphene has a fourfold degeneracy from the spin and valley degrees of freedom, such that each Landau level $N \neq 0$ can accommodate four electrons or four holes and the zeroth LL is filled symmetrically with two electrons and two holes. From this a filling factor of the Landau levels ν_{LL} following a half-integer sequence $\pm 4\left(|N| + \frac{1}{2}\right) \rightarrow \pm 2, \pm 6, \pm 10...$ is defined such that the carrier density required to fill the energy states up to Landau level N is [34]

$$n_{LL} = \frac{B}{\phi_0} \cdot \nu_{LL}, \tag{4.4}$$

where $\phi_0 = \frac{h}{e}$ is the magnetic flux quantum.
For the LLs emanating from the Dirac point, twisted bilayer graphene is expected to have an eightfold half-integer quantum Hall sequence $\pm 4, \pm 12, \pm 20...$, which is double that of

single-layer graphene due to the presence of the second layer. This was indeed measured in devices with larger twist angle ~1.8° [33]. However, in the vicinity of magic-angle, it is observed that the degeneracy reduces from eightfold to fourfold with the sequence $\pm 4, \pm 8, \pm 12...$, possibly due to symmetry breaking [36].

Experimentally, Landau levels manifest as quantized plateaus in the transverse resistance R_{xy} accompanied by zero longitudinal resistance R_{xx} when the Fermi level lies between two LLs, as shown in Fig. 4.5. The plateaus at each level are given by [34]

$$R_{xy} = \frac{R_K}{\nu_{LL}}, \tag{4.5}$$

where $R_K = \frac{h}{e^2} \approx 25.812\,\mathrm{k\Omega}$ is the von-Klitzing constant.

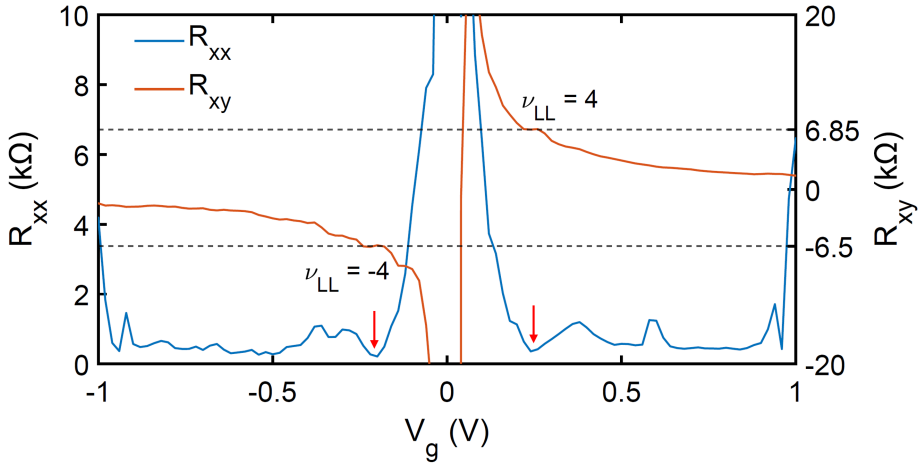

Figure 4.5: Magnetoresistance (R_{xx}) and Hall resistance (R_{xy}) vs. gate voltage. The traces are line cuts from the Landau fan in Fig. 4.6 taken at $B = 5\,\mathrm{T}$. The red arrows point to resistance minima in R_{xx} which are accompanied by resistance plateaus in R_{xy} at Landau filling factor $\nu_{LL} = 4$, where $\frac{R_K}{R_{xy}} \approx 4$.

Twist angle determination

By measuring the longitudinal(and transverse) resistance as a function of V_g and B, we obtain a so-called Landau fan (Fig. 4.6) in which we can identify the different Landau levels as "lines" emanating from the different states of TBG. By identifying the most prominent Landau level emanating from the CNP (usually $\nu_{LL} = 4$ in TBG) and calculating the slope $\frac{\Delta B}{\Delta V_g}$ along it, we can extract the gate capacitance combining Eq. 4.1 and Eq. 4.4:

$$C_g = \frac{e^2}{h} \frac{\Delta B}{\Delta V_g} \cdot \nu_{LL}. \tag{4.6}$$

To identify $\nu_{LL} = 4$, we find the plateau value in R_{xy} which is consistent with $\frac{R_K}{4} \approx 6.45\,\mathrm{k\Omega}$ accompanied by a resistance minimum in R_{xx}. We then find the slope $\left(\frac{\Delta B}{\Delta V_g}\right)_{\nu_{LL}=4}$ that not only accurately fits the $\nu_{LL} = 4$ level but also enables a correct reconstruction of the LL sequence, as will be explained shortly. This method yields $C_g = 333 \pm 6\,\mathrm{nF/cm^2}$.

The position of the band insulator for this region is accurately determined by finding the intersection point of the Landau levels emanating from it, which we find to be $V_{BI} = 2.110 \pm 0.001\,\mathrm{V}$. With the above C_g we get a twist angle of $\theta = 1.37 \pm 0.01°$. We deduce that this configuration primarily reflects the characteristics of the region with a higher twist angle, although there is a hint to correlated insulating states at $V_{CI,e} = 0.55\,\mathrm{V}$ and $V_{CI,h} = -0.65\,\mathrm{V}$ in the Landau fan. In conclusion, we interpret the response of this device region as a mixed contribution from a larger twist angle and a near-magic-angle $\theta_{MA} = 0.99 \pm 0.06°$, estimated from the center of the CI and the above C_g, which is consistent with the previous two-probe estimation.

Landau level reconstruction

The quantum Hall sequence of the LLs diverging from the CNP is reconstructed by first fitting the previously identified $\nu_{LL} = 4$ state and extracting its corresponding slope $m_{\nu_{LL}=4} \coloneqq \left(\frac{\Delta B}{\Delta V_g}\right)_{\nu_{LL}=4}$. Since $\frac{B}{V_g} \propto \frac{1}{\nu_{LL}}$, we calculate the slope of the next Landau levels as $m_{\nu_{LL}} = m_{\nu_{LL}=4} \cdot \frac{4}{\nu_{LL}}$, where ν_{LL} match their corresponding Hall plateaus in R_{xy} and are consistent with the expected values for (twisted bilayer)graphene (Supplementary data, Table A.2). The fitted lines then align correctly with the resolved Landau levels in the Landau fan, as can be seen in Fig. 4.6. On the electron side, the expected sequence for magic-angle $+4, +8, +12...$ is observed, with $+28$ missing. Applying the same analysis to the hole side, we identify levels corresponding to the magic-angle sequence ($-4, -12, -16, -20$, with -8 missing), higher angle ($-28, -36$) and single-layer (-6, -10). The degeneracy of the LLs emanating from the BI could not be identified because the R_{xy} plateaus could not be resolved.

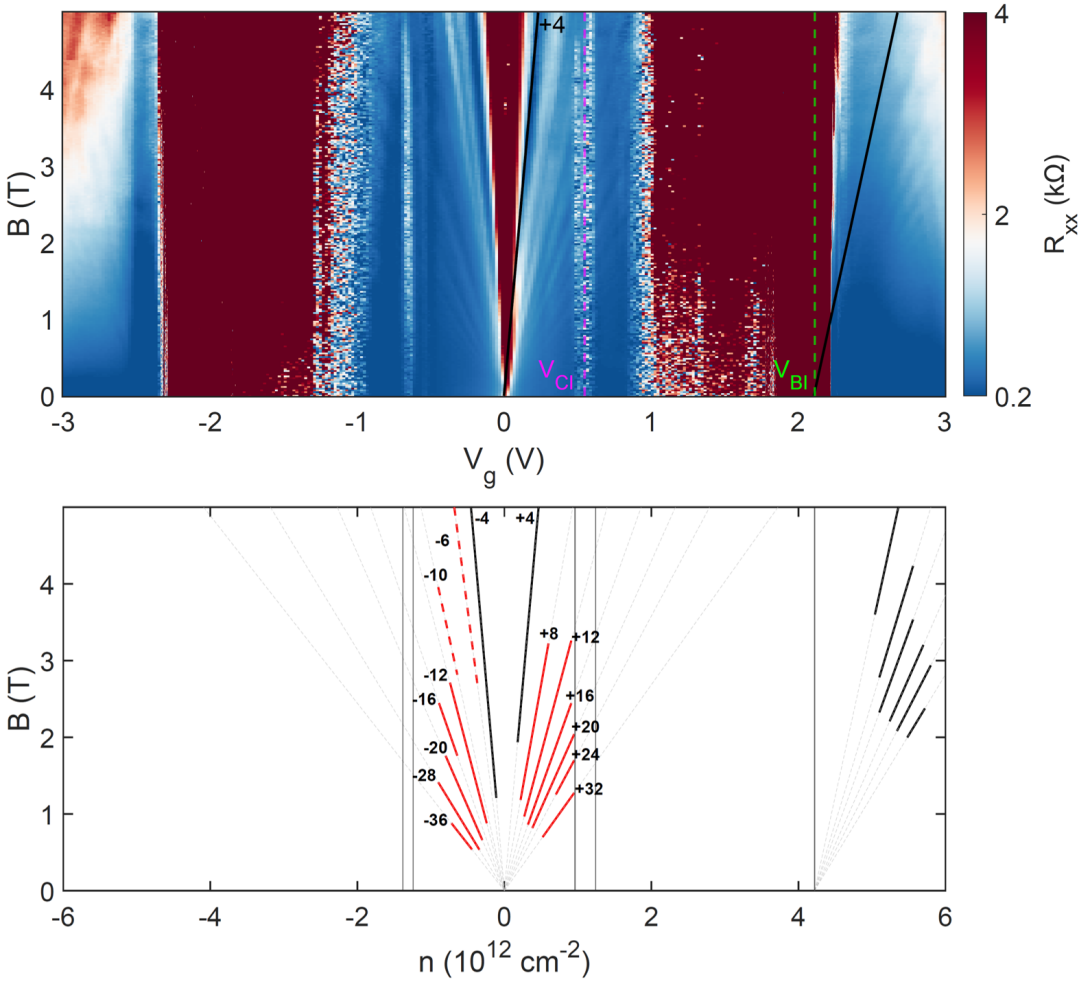

Figure 4.6: Landau fan diagram. Top, color map of longitudinal resistance vs. gate voltage and magnetic field at $T = 300\,\mathrm{mK}$. The twist angle $\theta = 1.37°$ is determined from $\left(\frac{\Delta B}{\Delta V_g}\right)_{\nu_{LL}=4}$ and V_{BI}. V_{CI} is the central position of the correlated insulator corresponding to $\theta = 0.99°$. Bottom, reconstructed Landau level structure emerging from the CNP. The LLs originating from the BI do converge at V_{BI} but their degeneracy could not be determined due to unresolved plateau values.

5 Thermoelectric transport in the TBG device

After characterizing the TBG device in terms of twist angle and magneto-electrical properties, we proceed to investigate its thermoelectric response using the measurement scheme described in Section 3.3. The first section presents a detailed analysis of the heating scheme induced by the heater on bottom hBN-graphite, which is the main goal of this thesis. Insights from this analysis are then utilized to extract the Seebeck coefficient of the device in Section 5.2. Additionally, we examine the dependence of the measured thermovoltage signal on various measurement parameters to optimize it for accurate physical interpretation. The final two sections provide a brief comparison between the optimized thermovoltage traces and the behavior predicted by the Mott formula (Section 5.3). A presentation of the acquired data of thermovoltage in the presence of a magnetic field is then provided, accompanied by brief commentary (Section 5.4). An in-depth understanding of the last results is outside the scope of this thesis and would represent the next phase of this project.

5.1 Temperature gradient estimation

Since we aim to measure the thermopower between the pairs of probes which are within the magic-angle region, we attempt an estimation of the local temperature induced by the heater at each pair (see schematic in Fig. 5.1A), by utilizing the temperature dependence of the pronounced correlated insulator resistance peak at $\nu = +2$ discussed in Chapter 4. Previous studies report thermal activation gaps of 0.2–0.9 meV for these states [2, 5, 37], making them sensitive to temperatures between a few hundred mK to a few K, which corresponds to the temperature range where we aim to operate to study correlated physics in MATBG. As mentioned in the design section (Section 3.2), the close spacing of the probes in each pair minimizes positional error, enabling a more accurate reconstruction of the temperature profile across the device length.

5.1.1 Measurement procedure and results

The measurement procedure is similar to [7], where the peak resistance is measured as a function of fridge temperature T and applied DC current I_h through the heater on bottom hBN-graphite, while the heater on SiO_2 is off. Both resistances for pairs 2 and 3 were measured simultaneously in a four-probe configuration, while pair 1 was separately measured in two-probe, since it corresponds to the outermost contacts on one side of the

device. This difference, along with the disorder discussed in the previous chapter, may contribute to a reduced quality of the estimation.

Fig. 5.1B shows the resulting color maps of resistance vs. heater current and fridge temperature at $V_g = 0.6\,\mathrm{V}$ for each pair. The contour lines of same resistance trace (I_h, T) configurations that result in the same local temperature, which is the intercept of the contour line with the T-axis: $T_{local} = T_{contour}(I_h = 0)$. For instance, at pair 2, a heater current of about $50\,\mu\mathrm{A}$ at a fridge temperature $T = 50\,\mathrm{mK}$ induces a local temperature of about $T_2 = 0.8\,\mathrm{K}$. To determine the temperature difference between the pairs, we extract the local temperature at each pair for identical measurement conditions (I_h, T) and we expect to find $T_1 > T_2 > T_3$, where T_1 is the closest pair to the heater and T_3 is the farthest one. While this trend is not immediately apparent from the color maps, a closer examination reveals a temperature difference $\Delta T_{23} = T_2 - T_3 \approx 0.8\,\mathrm{K} - 0.7\,\mathrm{K} \approx 100\,\mathrm{mK}$ for $(I_h, T) = (50\,\mu\mathrm{A}, 50\,\mathrm{mK})$. The limited resolution of ΔT in this case arises from the small spatial separation between the pairs (~$1.5\,\mu\mathrm{m}$), reducing the temperature difference to values that fall below the calibration's resolution. Notably, the difference between the further pairs T_1 and T_3 is more pronounced than between the closer pairs T_1 and T_2.

To understand what limits our calibration's resolution, we look at the activation gaps associated with each pair, which we find to be $\Delta_1, \Delta_2, \Delta_3 = 0.08, 0.12, 1.6\,\mathrm{meV}$ respectively. This difference in energy gap essentially means that we are using "thermometers" with different sensitivities that only partially overlap to provide a correct ΔT estimation. Since we would like to achieve a small ΔT to remain within the linear response regime, an ideal scenario would be to have the same gap across all three pairs, for example $\Delta \approx 0.12\,\mathrm{meV}$, which shows to be most sensitive between $0.5\,\mathrm{K}$ and $1.5\,\mathrm{K}$ (Fig. 5.2B). In that case, the color map of the region farther from the heater would be "stretched" solely along the I_h-axis as compared to the closer region, reflecting the increased heater current required to reach the same temperature as the closer pair. Such a configuration can be achieved with a more homogeneous device exhibiting the same gap across the length of the device, suggesting that this calibration method is viable but ultimately limited by device inhomogeneity. A comparison between the ideal case and the experimental data is shown in Fig. 5.2. Another possibility for the device at hand is to repeat the calibration using the second heater on the opposite side of the device (placed on the SiO_2 substrate): in this configuration, the pair with the larger gap of $1.6\,\mathrm{meV}$ is positioned closer to the heater, making it a sensitive thermometer for higher temperatures, while the farther pair with the smaller gap of $0.12\,\mathrm{meV}$ is more sensitive to lower temperatures.

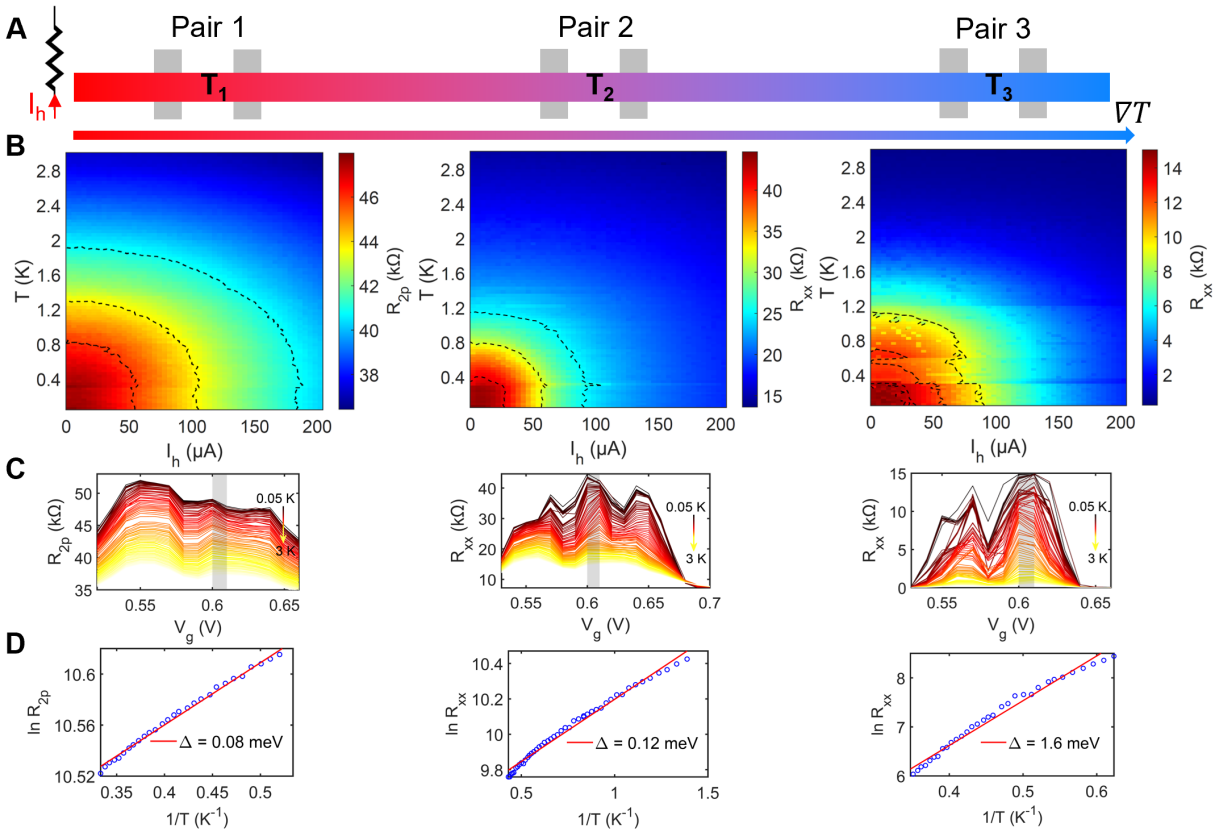

Figure 5.1: Temperature calibration. **A**, Schematic of the device. The heater on bottom hBN-graphite induces local temperatures T_1, T_2, T_3 when applying a heater current I_h through it. The heater on the other side of the device is off. The distance from the heater to the first probe in pair 1 is ~3 µm, both the probe width and the distance between each two probes in one pair are 0.5 µm and the smallest distance between the pairs is 1.5 µm. **B**, Color maps of resistance vs. heater current and fridge temperature for the three pairs of probes, from closest to heater (T_1) to farthest (T_3). The lowest temperature is 50 mK. The black dashed lines are contour lines of same resistance from which the local temperature can be extracted (explained in the text). **C**, Temperature dependence of the resistance vs. gate voltage within the half-filled CI. The shaded gray area is the point for which the corresponding color maps are plotted ($V_g = 0.6$ V). **D**, $\ln(R)$ vs. inverse temperature $1/T$ for the half-filled CI. The thermal activation gaps, for which $R \propto \exp(\Delta/2k_BT)$ holds, are determined from the fit for each pair.

5.1.2 Temperature mapping and error estimation

To quantify the uncertainty in the estimated temperature difference and identify the range of heater current where the estimation is most reliable, we map heater current to temperature through $T \to R(T) \to R(I_h) \to I_h$, using line cuts $R_{I_h=0}(T)$ and $R_{T=50\,\mathrm{mK}}(I_h)$. The resistance profiles $R(T)$ and $R(I_h)$ exhibit a clear trend, which we model using a third-degree polynomial fit. By carefully selecting the fitting range, we ensure that the polynomial captures the underlying trend without introducing artifacts (Fig. 5.2B). Unlike

piecewise interpolation, which strictly adheres to individual data points and may amplify measurement noise or anomalies, polynomial fitting preserves the global trend in this case, ensuring a smooth and physically meaningful reconstruction of the T vs. I_h map. The implementation details of the mapping procedure can be found in the MATLAB code

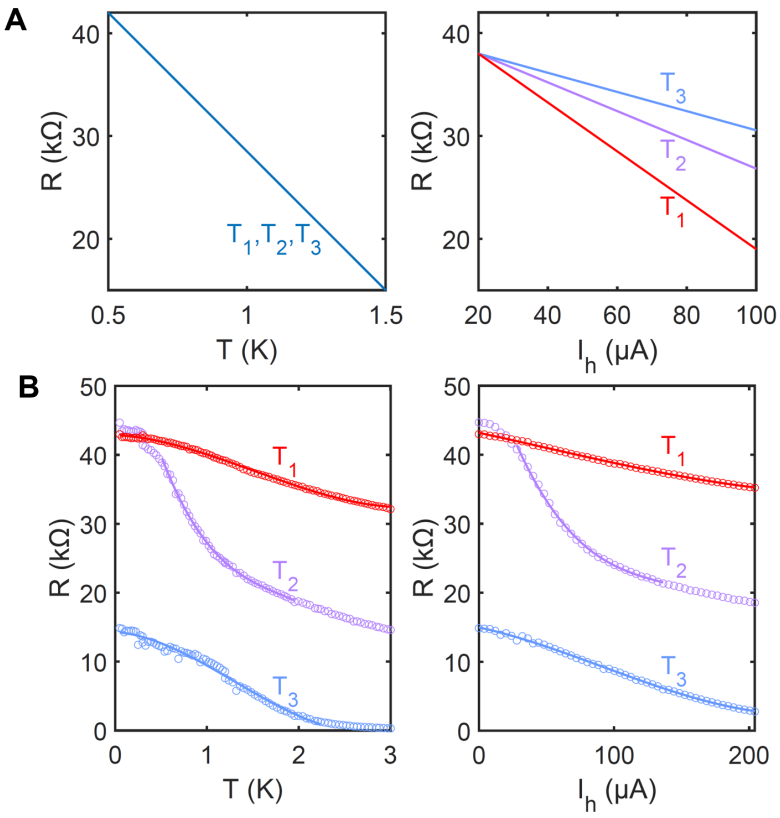

Figure 5.2: **A**, Ideal resistance dependence on temperature (left) and heater current (right) for pair 1,2,3, used as thermometers that extract local temperatures T_1, T_2, T_3 respectively. In this case, all three thermometers share the same sensitivity dR/dT over some temperature range, and the decreasing slope in R vs. I_h indicates $T_1 > T_2 > T_3$ from closest to farthest pair to the heater. To simply illustrate an ideal case, we show both a linear thermometer and R linear in I_h, but they can have different dependencies. **B**, Measured $R_{I_h=0}$ vs. T (left) and $R_{T=50\,\mathrm{mK}}$ vs. I_h (right), with third-degree polynomial fits for each pair. It can be seen that each pair has a different sensitivity in T, making the calibration accurate only for a restricted I_h and T range.

provided in Appendix B. The error on the mapped T values is estimated through error propagation as follows:

$$\sigma_T = \frac{\mathrm{d}T}{\mathrm{d}R}\sqrt{\sigma^2_{R(T)} + \sigma^2_{R(I_h)} + \sigma^2_{R_{map}}}, \tag{5.1}$$

where $\sigma_{R(T)}$ and $\frac{\mathrm{d}T}{\mathrm{d}R}$ are respectively the residual and the inverse of the derivative of the polynomial fit for $R(T)$ at the closest measured T to the mapped value. $\sigma_{R(I_h)}$ is the residual at the corresponding I_h and $\sigma_{R_{map}}$ is the difference between the fitted values of

$R(T)$ and $R(I_h)$ at each mapping point. This total error captures both the quality of the fit and map as well as the sensitivity through the term $\frac{dT}{dR}$. The result is shown in Fig. 5.3. While we do see the expected trend $T_1 > T_2 > T_3$ going from closest to farthest pair, it is most consistent in the range $50 - 70\,\mu A$ where the error bars are also the lowest. The obtained values for that range are

$$T_1 = 930 \pm 10\,\text{mK},\ T_2 = 875 \pm 10\,\text{mK},\ T_3 = 745 \pm 20\,\text{mK},$$

resulting in temperature differences of

$$\Delta T_{12} = 54\,\text{K} \pm 30\%,\ \Delta T_{23} = 130\,\text{K} \pm 15\%,\ \Delta T_{13} = 184\,\text{K} \pm 10\%,$$

where $\Delta T_{ij} = T_i - T_j$ and the relative error is $\sqrt{\sigma_{T_i}^2 + \sigma_{T_j}^2}/\Delta T_{ij}$.

Looking at the relative errors, we disregard ΔT_{12} and use the other two values as reasonable estimates for the following discussion.

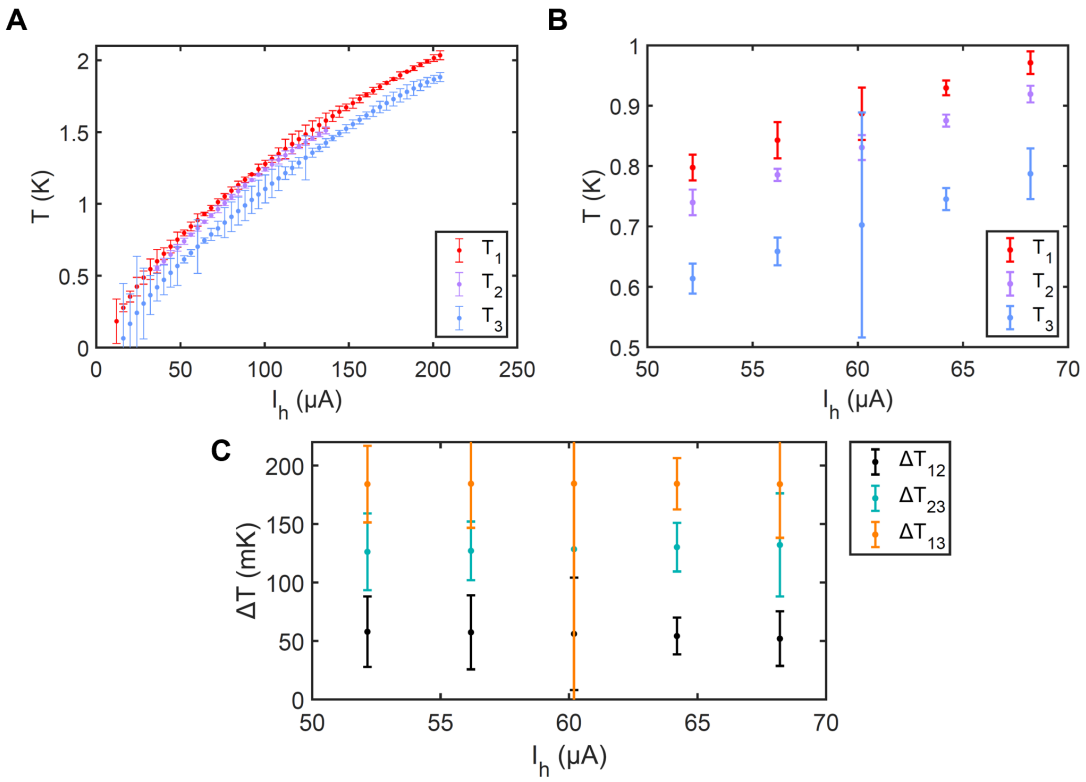

Figure 5.3: Temperature mapping and error estimation. **A**, Mapped local temperature T for each heater current I_h at each pair. **B**, Zoomed-in view of T vs I_h in the range where the calibration is valid. **C**, Corresponding temperature difference ΔT vs. I_h for all pair combinations.

5.1.3 Key conclusions about the measurement scheme

We conclude that this rough calibration has provided valuable insights into our measurement scheme at low temperatures (1 K and below), insights that were previously unattainable with our single-layer graphene test devices. Traditionally, thermoelectric measurements on SLG are conducted at higher temperatures (above ~3 K) using gold thermometers [14, 38]. More advanced techniques, such as Johnson noise thermometry [5], can be employed to achieve more precise low-temperature measurements.
Our findings for the configuration ($T_{fridge} = 50\,\mathrm{mK}$, $I_h = 60 \pm 10\,\mu\mathrm{A}$) are summarized in the following points. The same analysis can be applied for other configurations.

- **Temperature gradient and cooling length.** We have now estimated the local temperatures as well as the temperature gradient induced by the heater placed on bottom hBN-graphite (see heater dimensions in Fig. 3.9), proving that it efficiently heats the sample. Fig. 5.4B suggests that ΔT decreases with device length, resulting in an estimated cooling length of approximately 8 µm, with the heater placed ~3 µm from the first TBG probe. Under the assumption of a linear temperature gradient, we find $|\boldsymbol{\nabla} T| \approx 30\,\mathrm{mK/\mu m}$ (Fig. 5.4A).

- **Linear response regime.** Since we are interested in the linear response of the system, where $\Delta T \ll T$ and the Seebeck coefficient is $\Delta V = -S\Delta T$, with this estimation we find $\Delta T_{23} \approx 130\,\mathrm{mK} < T_3 \approx 745\,\mathrm{mK}$. Here, we compare the temperature difference to the estimated local temperature of the "cold side" and not to the fridge temperature, since the "cold" contact is not physically anchored to the fridge's base temperature. Given that our estimation is not very precise, we additionally make sure that the thermovoltage is measured in the linear regime by selecting a heater current in the range where V_{th} is linear in heating power $P_{Joule} = RI_h^2$, i.e., $V_{th} \propto I_h^2$. At $T_{fridge} = 50\,\mathrm{mK}$, we see this dependence for V_{th} between pair 2 and pair 3 up to around 50 µA (Fig. 5.8). Since our I_h range from the calibration lies right at the edge of this "linear" range, we take $I_h = 50\,\mu\mathrm{A}$ and use the corresponding estimated $\Delta T \approx 100\,\mathrm{mK}$ to calculate the Seebeck coefficient.

- **Magnitude of the Seebeck coefficient.** With a measured thermovoltage of $V_{th} = 1\text{-}2\,\mu\mathrm{V}$ at the peak value around the Dirac point and $\Delta T = 100\,\mathrm{mK}$ we obtain a magnitude of $S = 10 - 20\,\mu\mathrm{V\,K^{-1}}$ (Fig. 5.9), consistent with literature values for twisted bilayer graphene [5].

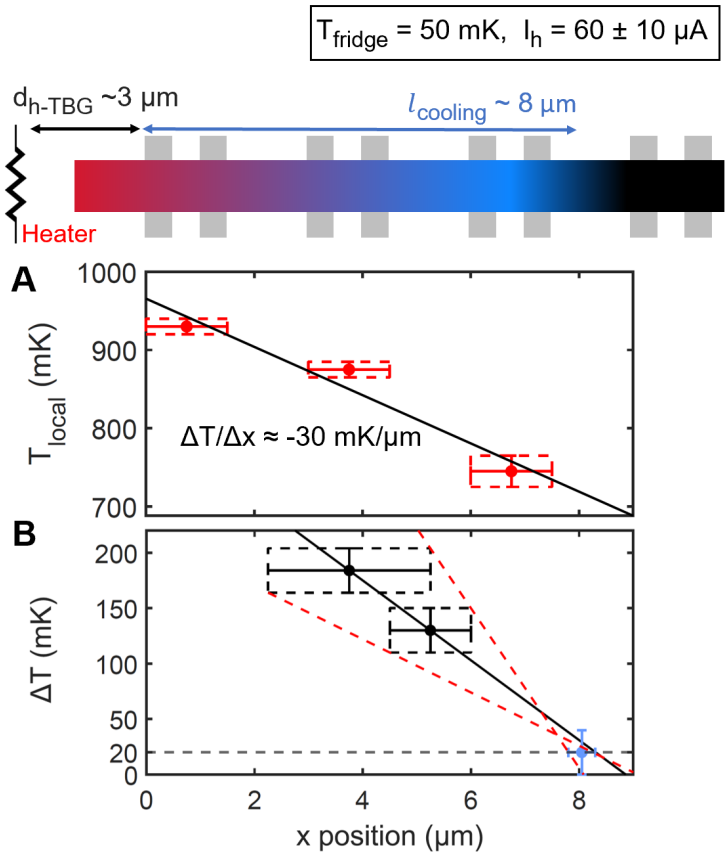

Figure 5.4: Temperature profile. **A**, Local temperature at each pair vs. x-position as defined in the device schematic (top), for heater 1 on bottom hBN-graphite, $T_{fridge} = 50\,\text{mK}$ and $I_h = 60 \pm 10\,\mu\text{A}$. Under the assumption of a linear temperature profile, we find $|\boldsymbol{\nabla} T| = 30\,\text{mK}/\mu\text{m}$ from the linear fit of the data points. **B**, Rough estimation of the cooling length. To find $l_{cooling}$, we assign the estimated ΔT between each pair of thermometers to the midpoint between them, with the error bar in the x-position spanning the distance between them. We then identify where the three resulting temperature profiles intersect the 20 mK line, such that $l_{cooling} = x(\Delta T = 20\,\text{mK}) \approx 8\,\mu\text{m}$. Temperature differences below 40 mK are considered negligible.

5.2 Thermovoltage signal optimization

Our next focus is on the thermoelectric response between pairs 2 and 3, where the thermovoltage (V_{th}) is measured following the method described in Section 3.3, with heater 1 on. Key considerations for accurate measurement include selecting the appropriate heater current and frequency to ensure operation within the linear response regime and capture both the signal's magnitude and sign.

5.2.1 Dependence on heater current and gate voltage

A heater current I_h ranging from 0 to 80 µA is applied and the resulting thermovoltage is measured as a function of gate voltage. At a fridge temperature of 40 mK, a detectable signal emerges at around 10 µA, as shown in Fig. 5.5A. Distinct features in the thermovoltage appear at specific gate voltages, which correlate with corresponding features in R_{xx}, particularly the zero-crossing at charge neutrality. This confirms that we are looking at the desired response. At zero heater current, gate-dependent fluctuations are observed (Fig. 5.5B), where they are largest at the high resistance states (charge neutrality, correlated insulator and band insulators), ranging from 50 to 100 nV. These fluctuations are superimposed on the thermoelectric signal at finite heater currents, complicating the interpretation of the signal at those states. An additional disturbance comes from fluctuations of around 10 pA in the gate leakage current (Fig. 5.5C), introducing "wiggles" in the signal. These are likely due to capacitive coupling between the heater's AC electric field and the graphite gate.

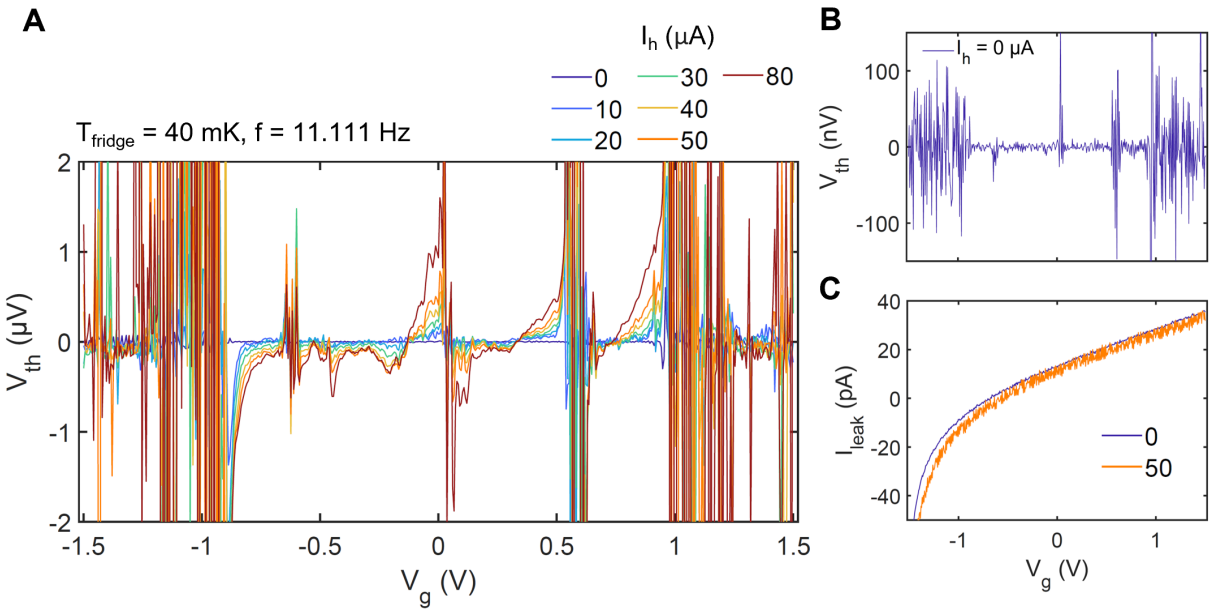

Figure 5.5: **A**, Thermovoltage V_{th} vs. gate voltage V_g for different heater currents. **B**, Zoomed-in view of V_{th} vs. V_g at zero heater current, showing gate-dependent fluctuations. **C**, Gate leakage current I_{leak} vs. V_g for zero heater current and for $I_h = 50$ µA, revealing additional fluctuations at finite I_h.

5.2.2 Dependence on heater current frequency

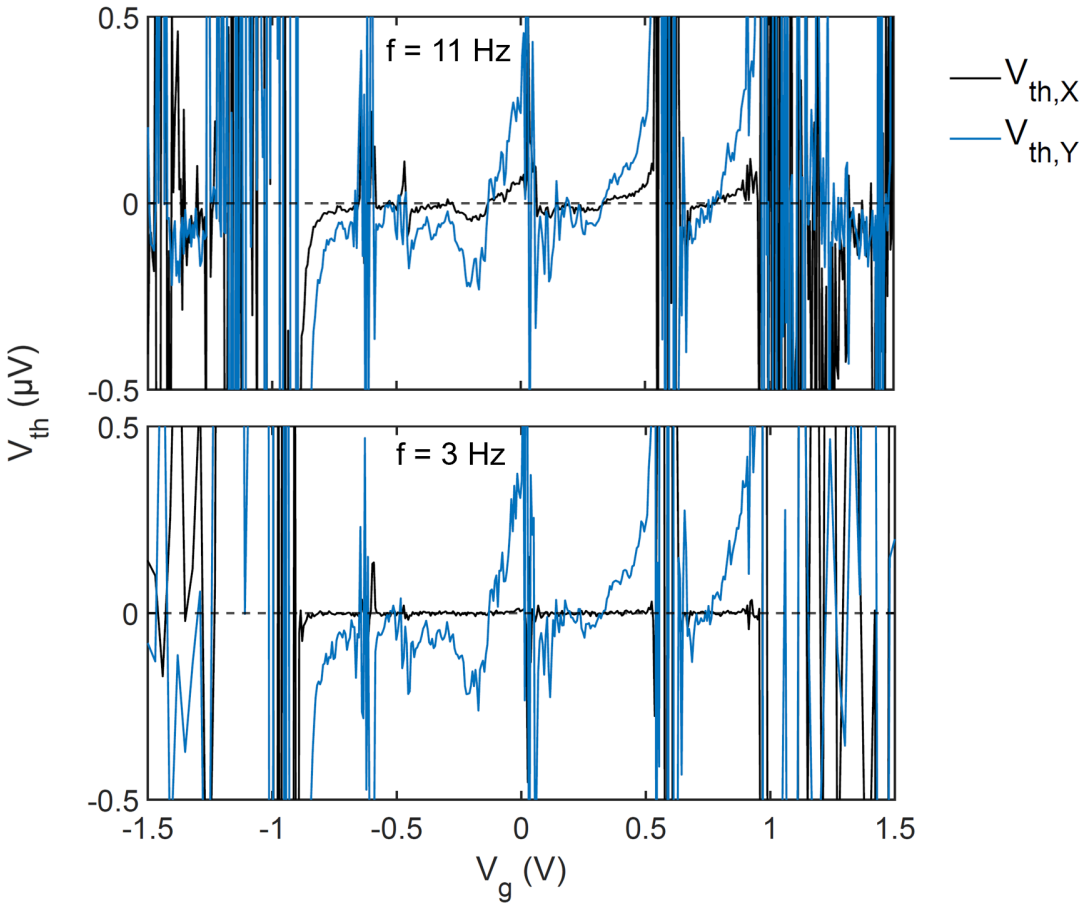

Figure 5.6: X and Y components of the measured thermovoltage for two different frequencies $f = 3\,\mathrm{Hz}$ and $f = 11\,\mathrm{Hz}$. The measurement was taken at 40 mK and $I_h = 35\,\mu\mathrm{A}$.

As discussed in Section 3.3, selecting an appropriate heating frequency facilitates signal interpretation. In Fig. 5.6, we see that at $f = 3\,\mathrm{Hz}$, the entire thermovoltage signal appears in the Y channel of the lock-in amplifier, whereas for a "higher" frequency of 11 Hz, a small but noticeable portion of the signal appears in the X-channel. Moreover, the phase remains most stable at 90° for $f = 3\,\mathrm{Hz}$ (Fig. 5.7B), further supporting this choice. Examining the frequency dependence of the thermovoltage across different gate voltages, we find that at charge neutrality and at half-filling on the hole side, the signal magnitude remains unchanged with frequency. Interestingly, however, at the correlated insulator on the electron side, the signal amplitude increases with frequency. Further investigation is needed to understand the reason for this, as it may stem from AC measurement artifacts due to a large temperature derivative of the thermopower $\mathrm{d}S/\mathrm{d}T$ at that state [5, 39]. Based on these observations, we use $f = 3\,\mathrm{Hz}$ for all subsequent measurements.

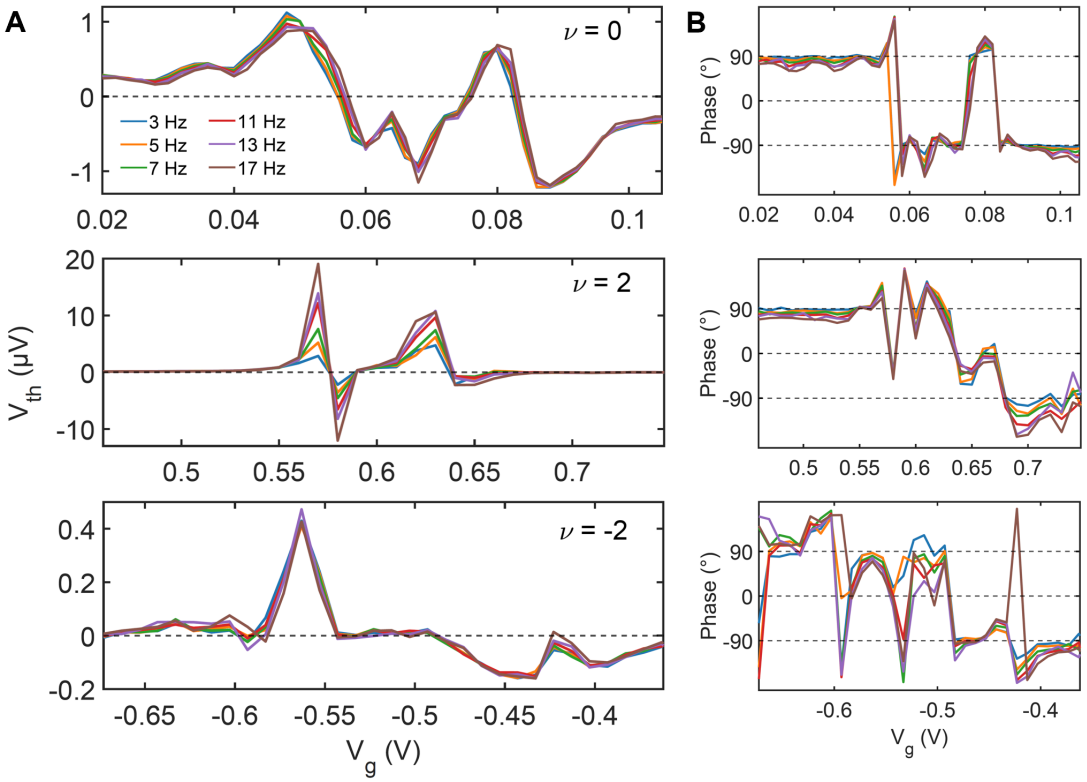

Figure 5.7: **A**, Frequency dependence of the thermovoltage around the Dirac point $\nu = 0$ and the half-fillings $\nu = \pm 2$. The filling factors are with respect to the 1° twist angle. **B**, Corresponding frequency dependence of the phase of the signal around each filling factor. The measurement was conducted at 1K and $I_h = 60$uA in a different cryostat than the previous measurements (Kiutra with 300 mK base temperature).

5.2.3 Linear response range at different temperatures

To ensure that the thermovoltage is measured in the linear regime, we record V_{th} as a function of heater current I_h at different gate voltages and select a heater current within the range where $V_{th} \propto I_h^2$. Since the induced temperature difference ΔT depends on the bath temperature, the same heater current might lie in the linear regime for one temperature, say 40 mK, but be too small to generate a measurable thermovoltage at a higher temperature. Conversely, a heater current that lies in the linear regime at higher temperatures may be too large for lower temperatures. This behavior can be seen in Fig. 5.8, where the range of $I_{h,\,linear}$ ends at around 50 µA for a bath temperature of 40 mK, while it ends at 65 µA at 1 K. This difference will be more noticeable when measuring at higher temperatures.

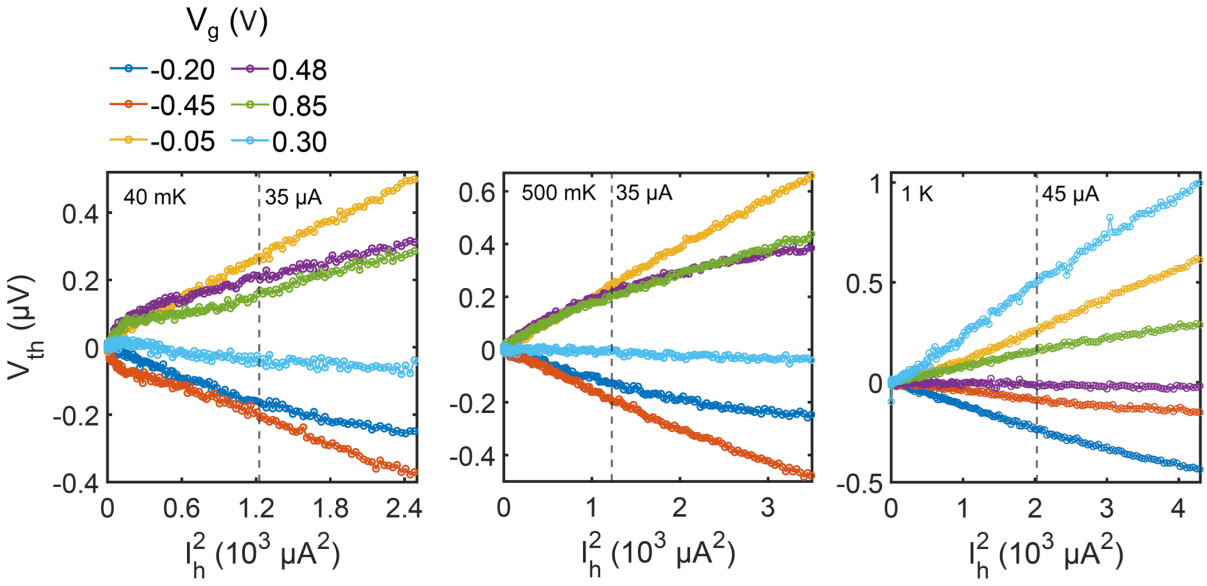

Figure 5.8: Thermovoltage V_{th} vs. I_h^2 at different gate voltages between $-1\,\mathrm{V}$ and $1\,\mathrm{V}$, for $T_{bath} = 40\,\mathrm{mK}$, $500\,\mathrm{mK}$ and $1\,\mathrm{K}$. The dashed lines in each plot indicate the selected heater current at which subsequent V_{th} vs. V_g traces will be measured, such that the response is within the linear regime.

5.2.4 Seebeck coefficient

After the above discussion, we present an optimized trace of the Seebeck coefficient vs. carrier density as well as a comparison with R_{xx} in Fig. 5.9. To obtain the magnitude, V_{th} was divided by the estimated $\Delta T = 100\,\mathrm{mK}$ for the corresponding configuration ($T_{bath} = 50\,\mathrm{mK}$, $I_h = 50\,\mu\mathrm{A}$). Since for this configuration, we saw that this heater current value lies just at the edge of the linear regime, we additionally provide the Seebeck at $I_{h,\,linear} = 35\,\mu\mathrm{m}$ for comparison. In both cases, the carrier density dependence is almost the same and the ΔT estimation provides a correct order of magnitude $10 - 20\,\mu\mathrm{V\,K^{-1}}$ around charge neutrality. The correspondence between the zero-crossing of the Seebeck and the Dirac peak in the resistance is clearly observed. Other features in S at different carrier densities might reveal information about the asymmetry in the electronic structure.

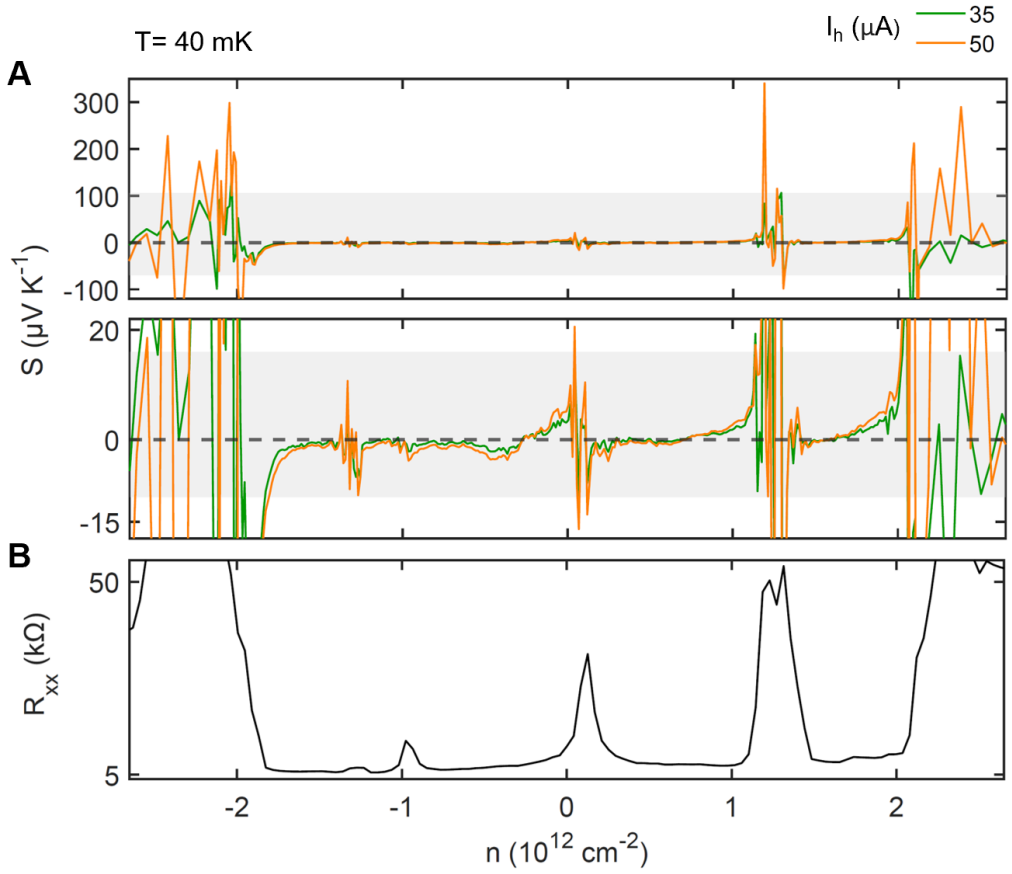

Figure 5.9: **A**, Seebeck coefficient S vs. carrier density n for heater currents 35 µA and 50 µA at 40 mK. The top plot shows a zoomed-out view of the trace and the bottom plot focuses on the smaller S values. The gray shaded area indicates the range of S for the lower heater current value. **B**, R_{xx} vs. carrier density showcasing the correspondence between thermopower and electrical resistance.

5.2.5 Comparison of the thermovoltage induced by two different heaters

So far, we have only used the heater placed on bottom hBN-graphite (heater 1), while heater 2 placed on the SiO_2 substrate was off. Here, we provide a brief comparison of the measured thermovoltage when heater 1 is off and heater 2 is on, and vice-versa. The thermovoltage is measured at three bath temperatures and in each case, the same heater current I_h is applied to both heaters, one at a time. We note in advance that I_h was optimized with respect to heater 1, and we do not have information about the heating scheme when using the SiO_2 heater. Still, we can compare the thermovoltage in each case to identify any differences. Looking at Fig. 5.10, at 40 mK and 500 mK, we see that both heaters result in a similar response for the whole range of gate voltages except near the half-filling on the hole side, around $V_g = -0.5$ V. Namely, heater 1 results

in a negative thermovoltage followed by a zero-crossing, while heater 2 results in two consecutive zero-crossings. At 1 K, the zero-crossing seems to disappear for heater 1 while it persists for heater 2. To understand these observations, the next step would be to repeat the same optimization measurements using heater 2, and compare the responses induced by the two heaters from lower to higher temperatures.

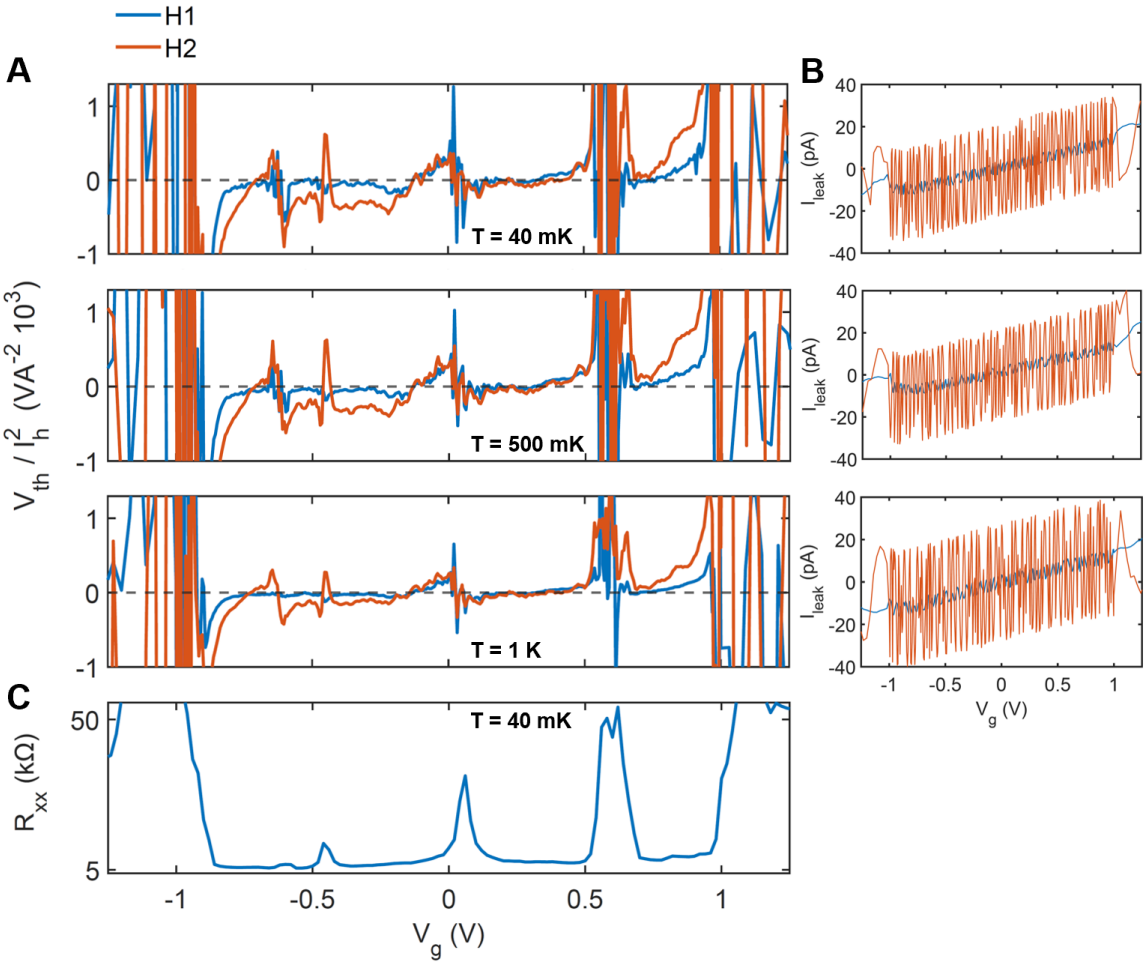

Figure 5.10: **A**, Comparison of the normalized thermovoltage V_{th}/I_h^2 induced by heater 1 on bottom hBN-graphite (H1) and by heater 2 on SiO_2 (H2), as a function of gate voltage. The measurement was repeated at three different fridge temperatures (40 mK, 500 mK and 1 K from top to bottom). **B**, Corresponding gate leakage current vs. V_g, suggesting that H2 "disturbs" the system more than H1. **C**, R_{xx} vs. V_g for comparison.

5.3 Comparison with the Mott formula

In this section, we compare the optimized thermovoltage vs. carrier density traces measured with heater 1 in two different setups (Bluefors fridge with base temperature 40 mK and Kiutra cryostat with base temperature 300 mK). Additionally, the thermovoltage measured in each setup is compared to the Mott formula using the corresponding R_{xx}.

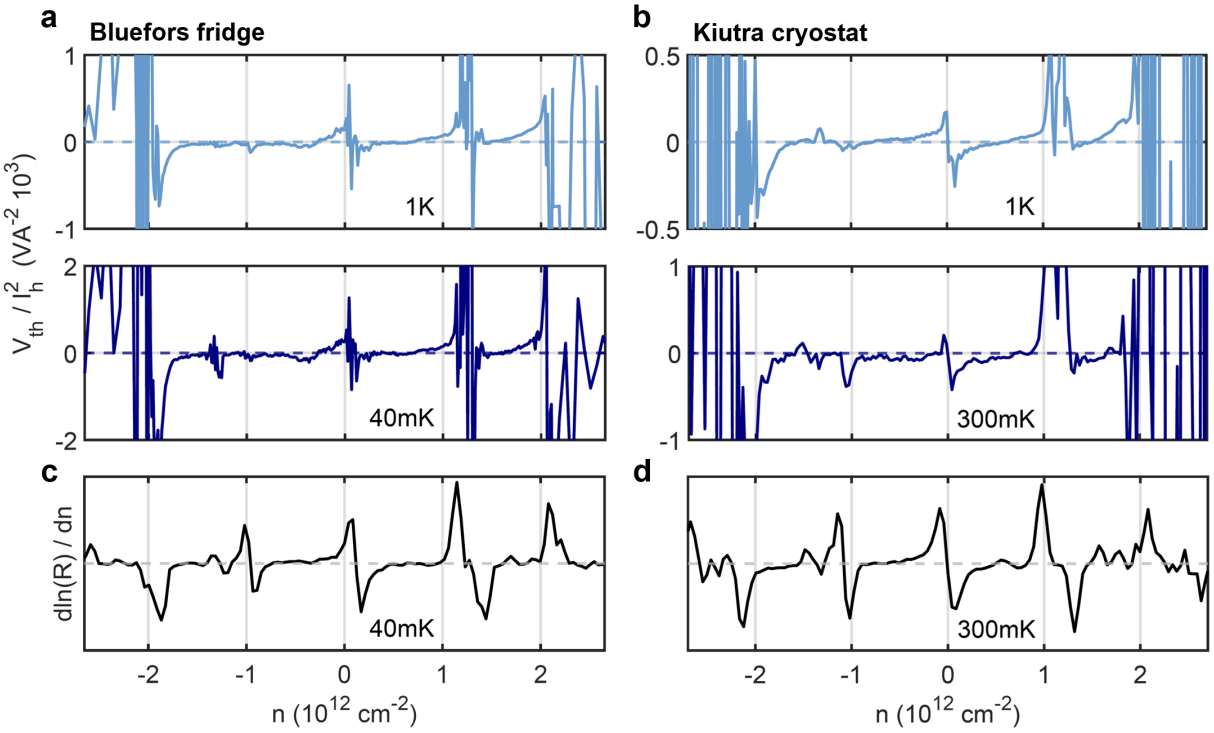

Figure 5.11: Comparison with the Mott formula. a, b, Normalized thermovoltage V_{th}/I_h^2 vs. carrier density in two different setups: the Bluefors fridge (**a**) and the Kiutra cryostat (**b**). In each case, the thermovoltage was measured at the respective base temperature and at 1 K. **c-d**, Numerically calculated $\mathrm{d}\ln(R)/\mathrm{d}n$ from the measured R_{xx} in Bluefors (**c**) and in Kiutra (**d**).

The Mott formula given in Eq. 2.25 can be rewritten in terms of resistance and density of states as follows: with $\ln\sigma = -\ln\rho = -\ln R + c$ and $\mathrm{d}\ln R/\mathrm{d}\varepsilon = (\mathrm{d}\ln R/\mathrm{d}n)g(\varepsilon)$, where $g(\varepsilon) = \mathrm{d}n/\mathrm{d}\varepsilon$ is the density of states, we obtain

$$S = \frac{\pi^2 k_B^2 T}{3e} \frac{\mathrm{d}\ln R}{\mathrm{d}n} g(\varepsilon)\Big|_{\varepsilon=\varepsilon_F}. \tag{5.2}$$

Note that c is a geometric factor in the resistance which vanishes when taking the derivative with respect to energy. This version of the Mott formula shows that in the semi-classical picture, the thermovoltage goes to zero at resistance maxima, where $\mathrm{d}\ln R/\mathrm{d}n = 0$. Since resistance maxima in MATBG occur at integer fillings of the flat band, zero-crossings are expected exactly there [5], as shown in Fig. 5.11c,d. While we do see the zero-crossing corresponding to charge neutrality in all cases, the Kiutra measurements (Fig. 5.11b) suggest that at half-filling on the electron side ($n \approx 1 \times 10^{12}\,\mathrm{cm}^{-2}$), the thermovoltage is fully positive both at 1 K and 300 mK. Similarly, at $n \approx -1 \times 10^{12}\,\mathrm{cm}^{-2}$, we do not observe a zero-crossing and instead the thermovoltage is fully negative. Such a deviation from the Mott formula in MATBG was observed in Ref. [5]. The Bluefors measurements show similar behavior, though at positive half-filling it is unclear whether the signal remains

fully positive or undergoes a reset, due to significant fluctuations. We also note that the actual electronic temperature in the Kiutra setup is likely higher than in the Bluefors fridge, despite both registering a bath temperature of 1 K. A temperature-dependent study within a single setup could provide further insights. The underlying reasons for these observations likely involve complex physics such as topological phase transitions and correlated phenomena [5, 6], which are beyond the scope of this thesis.

5.4 Thermovoltage in the presence of a magnetic field

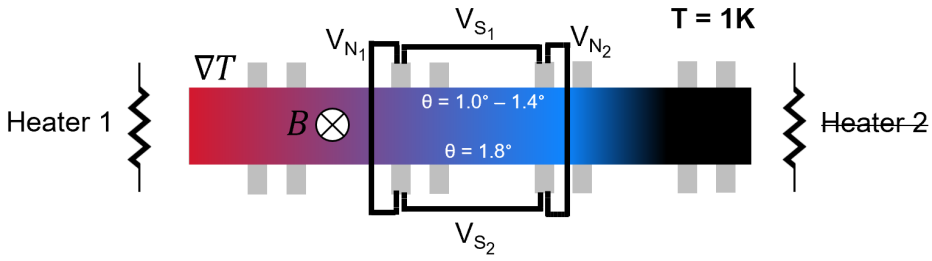

Figure 5.12: Schematic of the device for thermoelectric measurements in the presence of a perpendicular magnetic field. V_{S_i} and V_{N_i} refer to the Seebeck voltage (longitudinal) and Nernst voltage (transverse) respectively.

To further probe the properties of (MA)TBG, we perform thermoelectric measurements in the presence of a perpendicular magnetic field, where in addition to the longitudinal thermovoltage, information about the system can be gained from the transverse Nernst signal, which is the transverse electric field generated by a longitudinal thermal gradient in the presence of a magnetic field [7]. From Chapter 4, we know that the device at hand exhibits twist angle disorder, where one side of the device (the one we discussed so far in terms of V_{th}) shows correlated peaks from the 1° twist angle region, and the other side has a larger angle 1.8°. In this measurement, we probe the rectangular region shown in Fig. 5.12, where V_S refers to the longitudinal Seebeck voltage and V_N refers to the transverse Nernst voltage. The measurement was conducted in Kiutra at 1 K.

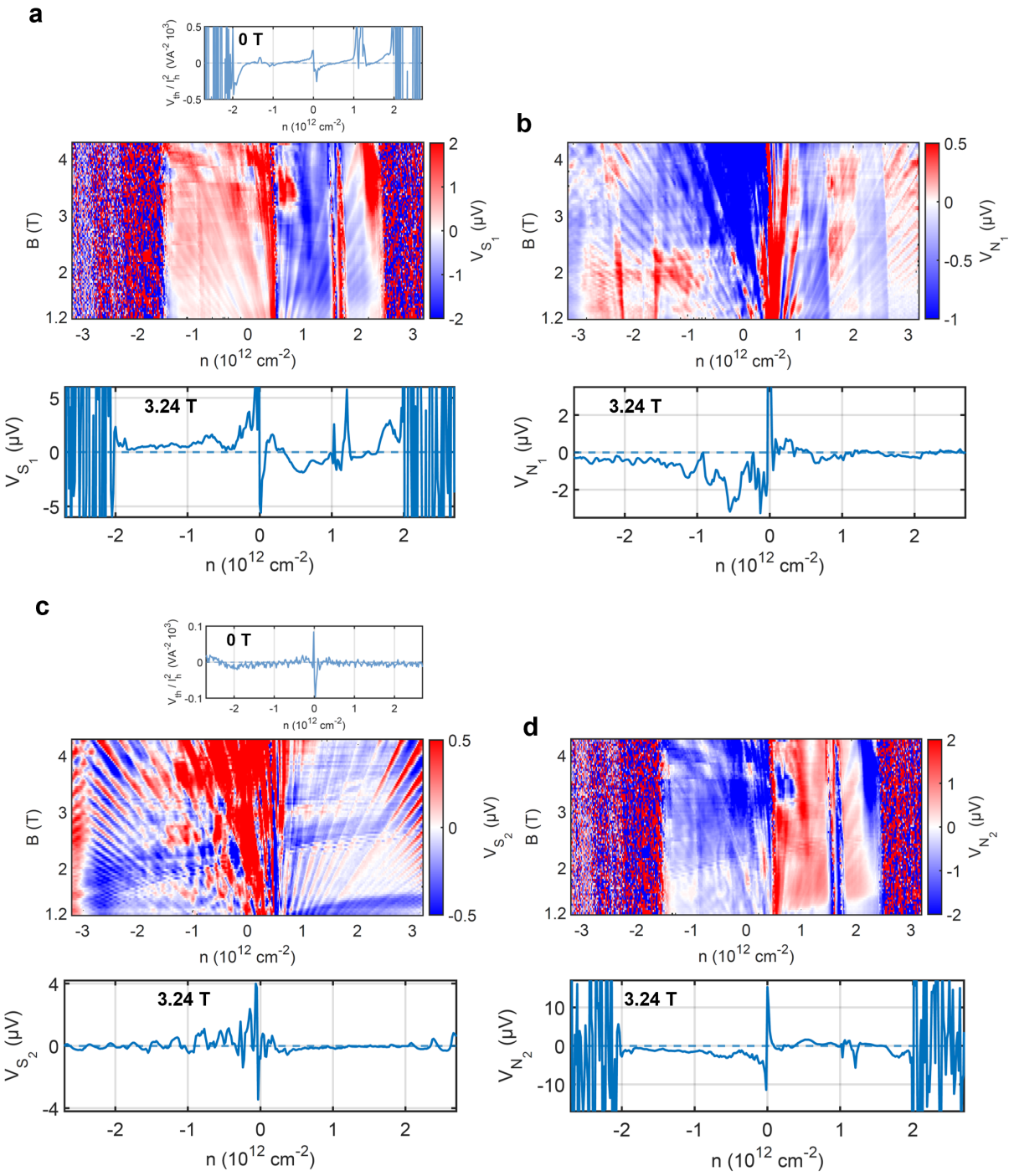

Figure 5.15: Seebeck and Nernst signals in the presence of a perpendicular magnetic field at 1 K. a,c, In each panel, the middle plot shows the color map of the Seebeck voltage V_{S_1} (a), V_{S_2} (c) vs. carrier density and magnetic field, from 4.28 T to 1 T. A map over the full magnetic field range could not be acquired due to instrumental constraints. The top plot shows the corresponding Seebeck at zero magnetic field and the bottom plot shows an exemplary line cut at 3.24 T. **b,d**, Color map of the Nernst voltage V_{N_1} (b) and V_{N_2} (d) vs. carrier density and magnetic field (top) and corresponding line cuts at 3.24 T (bottom).

The acquired data is summarized in Fig. 5.15. A multitude of oscillations can be seen in

both the Seebeck and Nernst signals. An in-depth analysis of the data is necessary to understand the origin of these oscillations, for example by calculating the corresponding $V_{S,\,Mott}$ and $V_{N,\,Mott}$ from R_{xx} and R_{xy} through the generalized Mott formula [14] and comparing them to the measured signals. To eliminate any potential signal mixing in the Nernst voltage due to geometric misalignment of the Hall arms, measurements at negative magnetic fields are necessary. Additionally, a direct interpretation of the Nernst signals is made complicated by twist angle disorder, as the voltage is measured between two microscopically distinct regions. Addressing these questions would be a natural next step in this project.

6 Conclusions and outlook

In the present work, we successfully developed a measurement scheme and protocol to access the thermoelectric properties of graphene devices. Specifically, we identified the key length scales necessary to establish a sufficient temperature gradient in a device, thereby inducing a measurable thermoelectric signal in the desired linear regime. The thermopower could be observed for the twisted bilayer graphene device at different temperatures, which allowed the analysis of the signal with respect to relevant measurement parameters such as heater current and frequency. In addition to that, the thermovoltage was compared to the Mott formula, revealing deviations at specific carrier densities. Further investigation can unveil whether measurement artifacts are present in our signal, for example by repeating the same temperature calibration and thermovoltage measurements with the heater placed on the SiO_2 substrate. Overall, many aspects in the measurement scheme can be further optimized, such as reducing the width and thickness of the microheater to achieve a higher resistance for Joule heating at low temperatures, improving device quality to enable a more straightforward and precise understanding of the heating scheme, and performing temperature-dependent measurements to observe potential changes in the thermovoltage signal. To conclude this thesis, we note that it is interesting to look at the magnetic-field dependent data and conduct further measurements over the full range of magnetic field to better understand the response both in the longitudinal and the transverse direction.

References

[1] Yang, S. Y. and Díez-Carlón, A. and Díez-Mérida, J. and Jaoui, A. and Das, I. and Battista, G. Di and Luque-Merino, R. and Mech, R. and Efetov, Dmitri K. Plethora of many body ground states in magic angle twisted bilayer graphene. *Low Temperature Physics* **49,** 631–639 (June 2023).

[2] Cao, Y. *et al.* Correlated insulator behaviour at half-filling in magic-angle graphene superlattices. *Nature* **556,** 80–84 (2018).

[3] Cao, Y., Fatemi, V., Fang, S. & et al. Unconventional superconductivity in magic-angle graphene superlattices. *Nature* **556,** 43–50 (2018).

[4] Wu, S., Zhang, Z., Watanabe, K. & et al. Chern insulators, van Hove singularities and topological flat bands in magic-angle twisted bilayer graphene. *Nature Materials* **20,** 488–494 (2021).

[5] Paul, A. K., Ghosh, A., Chakraborty, S., *et al.* Interaction-driven giant thermopower in magic-angle twisted bilayer graphene. *Nat. Phys.* **18,** 691–698 (2022).

[6] Ghawri, B., Mahapatra, P. S., Garg, M., *et al.* Breakdown of semiclassical description of thermoelectricity in near-magic angle twisted bilayer graphene. *Nature Communications* **13,** 1522 (2022).

[7] Song, T., Jia, Y., Yu, G., *et al.* Unconventional superconducting quantum criticality in monolayer WTe2. *Nature Physics* **20,** 269–274 (2024).

[8] Behnia, K. *Fundamentals of Thermoelectricity* (2015).

[9] Behnia, K. What is measured when measuring a thermoelectric coefficient? *Comptes Rendus. Physique* **23,** 25–40 (2023).

[10] Ghahari, F. *et al.* Enhanced Thermoelectric Power in Graphene: Violation of the Mott Relation by Inelastic Scattering. *Phys. Rev. Lett.* **116,** 136802 (13 2016).

[11] Kavokin, A. V., Portnoi, M. E., Varlamov, A. A. & Yerin, Y. Failure of Mott's formula for the thermopower in carbon nanotubes. *Phys. Rev. B* **109,** 235405 (23 2024).

[12] Castro Neto, A. H. and Guinea, F. and Peres, N. M. R. and Novoselov, K. S. and Geim, A. K. The electronic properties of graphene. *Rev. Mod. Phys.* **81,** 109–162 (1 2009).

[13] Li, G., Luican, A., Lopes dos Santos, J. M. B. & et al. Observation of Van Hove singularities in twisted graphene layers. *Nature Physics* **6,** 109–113 (2010).

[14] Zuev, Y. M., Chang, W. & Kim, P. Thermoelectric and Magnetothermoelectric Transport Measurements of Graphene. *Phys. Rev. Lett.* **102,** 096807 (9 2009).

[15] Moon, P. & Koshino, M. Energy spectrum and quantum Hall effect in twisted bilayer graphene. *Phys. Rev. B* **85,** 195458 (19 2012).

[16] Geim, A. K. & Grigorieva, I. V. Van der Waals heterostructures. *Nature* **499,** 419–425 (2013).

[17] Díez-Mérida, J. *et al.* High-yield fabrication of bubble-free magic-angle twisted bilayer graphene devices with high twist-angle homogeneity. *Newton* **0,** 100007 (2025).

[18] Huang, Y. *et al.* Reliable Exfoliation of Large-Area High-Quality Flakes of Graphene and Other Two-Dimensional Materials. *ACS Nano* **9,** 10612–10620 (2015).

[19] Blake, P. *et al.* Making graphene visible. *Applied Physics Letters* **91,** 063124 (2007).

[20] *LUTs - Non-destructive Image Enhancement.* Accessed 15 February 2025.

[21] Dean, C., Young, A., Meric, I., *et al.* Boron nitride substrates for high-quality graphene electronics. *Nature Nanotechnology* **5,** 722–726 (2010).

[22] Overweg, H. *et al.* Electrostatically Induced Quantum Point Contacts in Bilayer Graphene. *Nano Letters* **18,** 553–559 (2018).

[23] Purdie, D., Pugno, N., Taniguchi, T., *et al.* Cleaning interfaces in layered materials heterostructures. *Nat. Commun.* **9,** 5387 (2018).

[24] Uri, A., Grover, S., Cao, Y., *et al.* Mapping the twist-angle disorder and Landau levels in magic-angle graphene. *Nature* **581,** 47–52 (2020).

[25] Nam, N. N. T. & Koshino, M. Lattice relaxation and energy band modulation in twisted bilayer graphene. *Phys. Rev. B* **96,** 075311 (7 2017).

[26] Zomer, P. J., Guimarães, M. H. D., Brant, J. C., Tombros, N. & van Wees, B. J. Fast pick up technique for high quality heterostructures of bilayer graphene and hexagonal boron nitride. *Applied Physics Letters* **105,** 013101 (2014).

[27] Kamat, R. *et al.* Deterministic fabrication of graphene hexagonal boron nitride moiré superlattices. *Proceedings of the National Academy of Sciences* **121,** e2410993121 (2024).

[28] Köfferlein, M. *KLayout - Layout Viewer And Editor* Accessed: 2025-04-10.

[29] Karouta, F. A practical approach to reactive ion etching, journal = Journal of Physics D: Applied Physics. **47,** 233501 (2014).

[30] Wang, L. *et al.* One-dimensional electrical contact to a two-dimensional material. *Science* **342,** 614–617 (2013).

[31] Zurich Instruments. *Principles of lock-in detection and the state of the art* White Paper. Accessed: 2025-04-09 (2016).

[32] Bernevig, B. A. & Efetov, D. K. Twisted bilayer graphene's gallery of phases. *Physics Today* **77,** 38–44. ISSN: 0031-9228 (2024).

[33] Cao, Y. *et al.* Superlattice-Induced Insulating States and Valley-Protected Orbits in Twisted Bilayer Graphene. *Phys. Rev. Lett.* **117,** 116804 (11 2016).

[34] Ashcroft, N., Mermin, N. & Wei, D. *Solid State Physics* (2016).

[35] Giesbers, A. J. M. *et al.* Quantum-Hall Activation Gaps in Graphene. *Phys. Rev. Lett.* **99,** 206803 (20 2007).

[36] Zhang, Y.-H., Po, H. C. & Senthil, T. Landau level degeneracy in twisted bilayer graphene: Role of symmetry breaking. *Phys. Rev. B* **100,** 125104 (12 2019).

[37] Di Battista, G. *Towards infrared single-photon detection with superconducting magic-angle twisted bilayer graphene* PhD thesis (Ludwig–Maximilians–University, Munich, Germany, 2024).

[38] Duan, J. *et al.* High thermoelectricpower factor in graphene/hBN devices. *Proceedings of the National Academy of Sciences* **113,** 14272–14276 (2016).

[39] Logvenov, G. Y., Ryazanov, V. V., Gross, R. & Kober, F. Comment on "Anomalous peak in the thermopower of $YBa_2Cu_3O_{7-\delta}$ single crystals: A possible fluctuation effect". *Phys. Rev. B* **47,** 15322–15323 (22 1993).

A Supplementary data on electrical transport

Table A.1: Twist angle estimation with the method in Subsection 4.2.1.

Contact pair	$\theta(^\circ)$
14-5	1.0 ± 0.1
5-12	0.98 ± 0.07
12-6	0.98 ± 0.06
6-10	1.03 ± 0.08
10-1	1.15 ± 0.08
1-8	1.4 ± 0.1
18-9	1.77 ± 0.02
9-20	1.80 ± 0.05
20-11	1.80 ± 0.04
11-2	1.79 ± 0.04
2-4	1.75 ± 0.06
4-3	1.74 ± 0.05

Table A.2: Measured plateau values along $B(V_g)$ lines where the LLs are resolved in Fig. 4.6, for the electron (e) and hole (h) side. The closest value to the theoretical one is taken, with the error calculated as the mean absolute deviation around that value.

$\lvert\nu_{LL}\rvert$	$\lvert R_0/R_{xy}(e)\rvert$	$\lvert R_0/R_{xy}(h)\rvert$
4	3.95 ± 0.06	3.92 ± 0.03
6	–	4.8 ± 0.5
8	7.7 ± 0.1	–
10	–	9.8 ± 0.1
12	11.8 ± 0.3	11.3 ± 0.4
16	15.8 ± 0.4	15.85 ± 0.07
20	19.5 ± 0.3	19.2 ± 0.5
24	23.2 ± 0.3	–
28	–	27 ± 1
32	31 ± 1	–
36	–	34.9 ± 0.6

B MATLAB code for temperature gradient estimation

The following MATLAB code maps the applied heater current I_h to the temperature T via third-degree polynomial fits of the resistance vs. heater current and resistance vs. temperature traces. The same code can be used to find the map for the different pairs.

```
%% Input variables from imported data Ih, Rtp and T

j=9; % selected gate voltage
xIh = Ih(j,:); %measured Ih at T=50mK
yIh = Rtp(j,:,1); %measured R(Ih) at T=50mK
xT = squeeze(T(j,:)); %measured T at Ih=0
yT = squeeze(Rtp(j,1,:)); %measured R(T) at Ih=0

%% Third-degree polynomial fits over a selected range of xIh and
    xT respectively

%Ih
[xData, yData] = prepareCurveData( xIh, yIh );
ft = fittype( 'poly3' );
excludedPoints = excludedata( xData, yData, 'Indices', [1 2 3 4
   5 6 7 36 37 38 39 40 41 42 43 44 45 46 47 48 49 50 51 52] );
opts = fitoptions( 'Method', 'LinearLeastSquares' );
opts.Exclude = excludedPoints;
[fitresult, gof] = fit( xData, yData, ft, opts );

%T
[xDataT, yDataT] = prepareCurveData( xT, yT );
ft = fittype( 'poly3' );
excludedPointsT = excludedata( xDataT, yDataT, 'Indices', [1 2
   3 4 5 6 7 8 9 10 11 12 13 14 15 16 17 18 63 64 65 66 67 68 69
    70 71 72 73 74 75 76 77 78 79 80 81 82 83 84 85 86 87 88] );
optsT = fitoptions( 'Method', 'LinearLeastSquares' );
optsT.Exclude = excludedPointsT;
[fitresultT, gofT] = fit( xDataT, yDataT, ft, optsT );
```

```
26
27 %% Mapping
28 % Exclude unused data
29 xTexcl = xDataT(~excludedPointsT);
30 yTexcl = yDataT(~excludedPointsT);
31 xIhexcl = xData(~excludedPoints);
32 yIhexcl = yData(~excludedPoints);
33
34 % Generate fine x values and compute corresponding y using the
       fit
35 xTFine = linspace(min(xTexcl), max(xTexcl), 1000);
36 yTFine = feval(fitresultT, xTFine);
37 % Sort xFine and yFine in ascending order
38 [yTFine, sortIdx] = sort(yTFine);
39 xTFine = xTFine(sortIdx);
40
41 xIhFine = linspace(min(xIhexcl), max(xIhexcl), 1000);
42 yIhFine = feval(fitresult, xIhFine);
43
44 % Create an inverse interpolant T(R)
45 fitT_inverse = griddedInterpolant(yTFine, xTFine, 'linear', '
       none');
46
47 %T vs. Ih map
48
49 xIh_map = xIhexcl(~nan_indices); %Ih values
50 yIh_map = yIhexcl(~nan_indices);
51 xT_mapped_poly_Fine= fitT_inverse(yIhFine); %use interpolated R(
       Ih) values in inverse map T(R)
52 T_I_Map = griddedInterpolant(xIhFine, xT_mapped_poly_Fine, '
       linear', 'none'); % create map function based on that
53 T_Ih_mapped = T_I_Map(xIhexcl); %Final mapped T values
54 nan_indices = isnan(T_Ih_mapped);
55 T_Ih_mapped = T_Ih_mapped(~nan_indices); %remove nan elements
       outside of calibration range
56
57 %% Error estimation
58 % sigma_T residuals from R(T) fit
```

```
idx_closest_T = zeros(size(T_Ih_mapped));
for i = 1:length(T_Ih_mapped)
    [~, idx_closest_T(i)] = min(abs(xT - T_Ih_mapped(i))); % Find the closest xT for each T(Ih)
end
%Evaluate the fitted values for R(T) at the corresponding xT
yT_fit_closest = feval(fitresultT, xT(idx_closest_T));
%Calculate the residuals (difference between measured yT and fitted yT)
residuals_T = yT(idx_closest_T) - yT_fit_closest;
%Use residuals to estimate uncertainty on T(Ih)
sigma_RT = abs(residuals_T);

% Difference between fitted R(Ih) and R(T) values used for the same mapping point
delta_R = zeros(size(yIh_map)); % Initialize error array
yIh_eval_map = feval(fitresult, xIh_map); %match the size
%Find the difference
for k = 1:length(yIh_map)
    [min_diff, idx] = min(abs(yT_fit_closest - yIh_eval_map(k))); % Find closest measured R(T)
    delta_R(k) = min_diff; % Store the difference |R(T) - R(Ih)|
end

%sigma_RIh residuals from R(Ih) fit
sigma_RIh = abs(yIh_map - feval(fitresult, xIh_map));

%dT/dR inverse of derivative of R(T) fit
coeffsT = coeffvalues(fitresultT); % coeffs = [a3, a2, a1, a0] for poly3 fit
dR_dT = 3 * coeffsT(1) .* xT(idx_closest_T).^2 + 2 * coeffsT(2) .* xT(idx_closest_T) + coeffsT(3);
dR_dT = dR_dT'; %correct dimension
dT_dR = 1./dR_dT; %inverse

% Final error
err_T = abs(dT_dR) .*(sqrt(delta_R.^2+sigma_RIh.^2+sigma_RT.^2));
```

```
90
91 % Recap of final result: xIh_map are the Ih values used in the
       map (x-axis), T_Ih_Mapped are the mapped T values (y-axis),
       err_T is the total error on the mapped T values.
```